Cement and Concrete Composites 104 (2019) 103361

Contents lists available at ScienceDirect

Cement and Concrete Composites

journal homepage: www.elsevier.com/locate/cemconcomp

Influence of pore structure on the strength behavior of particle- and fiber-reinforced metakaolin-based geopolymer composites

Ange Therese Akono[a,b,*], Seid Koric[c], Waltraud M. Kriven[d]

[a] Department of Civil and Environmental Engineering, Northwestern University, United States
[b] Department of Mechanical Engineering, Northwestern University, United States
[c] National Center for Supercomputing Applications, University of Illinois at Urbana-Champaign, United States
[d] Department of Materials Science and Engineering, University of Illinois at Urbana-Champaign, United States

ARTICLE INFO

Keywords:
Geopolymers
Strength behavior
Nonlinear homogenization
Nanoporosity

ABSTRACT

Geopolymers are X-ray amorphous materials with appealing properties such as high flexural strength and high compressive strength. Yet, the influence of the heterogeneity and porosity on the constitutive behavior is not fully understood. We formulate a multiscale physics-based mechanistic model to describe the strength behavior of geopolymer composites. Using an energy-based approach, we derive novel solutions to describe the effective yield criterion of fiber-reinforced and particle-reinforced metakaolin geopolymers. We calibrate our theoretical model using nanoindentation tests and validate our theoretical framework via flexural strength tests on metakaolin-based geopolymer composites. Geopolymer composites are found to exhibit a pressure-dependent granular behavior. We subdivide the porosity into nanoporosity and microporosity. Our results indicate that the nanoporosity is solely influenced by the chemistry and is not influenced by the processing and the presence of reinforcement. Due tothe presence of nanoporosity, the strength-total porosity relationships are not unique. However, an approximate one-to-one correspondence exists between the strength and the microporosity. The nanogranular structure and the chemical composition at the nanometer scale have a profound influence on the effective mechanical response.Our conceptual framework is an important step in the mechanistic modeling of the behavior of geopolymer composites.

1. Introduction

Geopolymers are a class of inorganic polymeric and X-ray amorphous materials that consist of alumina, silica, and alkali metal oxides. They are synthesized by mixing a source of aluminosilicates (such as amorphous metakaolin) with a highly caustic alkaline and silica-rich solution. The synthesis occurs in three steps: (i) dissolution of the aluminosilicate source, (ii) polycondensation, and (iii) geopolymerization under ambient temperature [1–3]. Geopolymer composites exhibit many appealing properties such as: early strength development [4,5], low carbon dioxide footprint, high strength-to-weight ratio, high fracture toughness [6,7], high flexural strength, and high compressive strength [8,9]. However, mechanistic models are needed to fully understand the impact of a heterogeneous and multiscale microstructure on the stress-strain response for geopolymer composites.

A question not fully answered is the influence of microstructure and heterogeneity on the constitutive behavior of geopolymer binders reinforced with aggregates—particulates or fibers. On the one hand, a strong emphasis has been given to understanding and predicting the properties of geopolymer binders. For instance, systematic experimental studies have been carried out to understand the link between chemistry and mechanical composition for metakaolin-based geopolymer binders [8,9]. Phenomenological approaches have been developed to correlate the mechanical response to the chemistry of sodium-based metakaolin and fly-ash geopolymer binders either based on linear regression [10,11] or neural network models [12,13]. At the mesoscale, micromechanical approaches have been articulated that rely on statistical nanoindentation followed by linear or nonlinear upscaling [14,15]. However, these micromechanical models do not specifically address the interplay between nano- and microporosity and effective strength behavior.

On the other hand, finite element approaches have been formulated at the macroscopic scale to investigate the response of geopolymer concrete reinforced with steel rebars [16]. In those finite element simulations, the behavior of the geopolymer matrix was measured experimentally from uniaxial compression and flexural strength tests.

* Corresponding author. Department of Civil and Environmental Engineering, Northwestern University, United States.
E-mail address: ange-therese.akono@northwestern.edu (A.T. Akono).

https://doi.org/10.1016/j.cemconcomp.2019.103361
Received 25 February 2019; Received in revised form 28 May 2019; Accepted 2 July 2019
Available online 05 July 2019
0958-9465/

However, there is a need for mechanistic approaches to predict the behavior of metakaolin-based geopolymer composites with particulate or fiber reinforcement. Thus, our research objective is to formulate a rigorous physics-based and multiscale micromechanics-based theory that connects the elasto-plastic response of geopolymer composites to the heterogeneity and to the pore structure.

In this work, we formulate a nonlinear physics-based mechanistic model that describes the constitutive response of geopolymer composites and bridges the molecular and macroscopic length-scales. Using energy-based variational approaches such as the linear comparison composite method, we explore the influence of the nanogranular and particulate nature of geopolymer composites on the elasto-plastic constants. The manuscript is organized as follows: first we present our multiscale conceptual model for geopolymer, then we describe the evolution of the elastic and strength properties across multiple length-scales. We validate the model on unreinforced potassium geopolymer as well as particulate geopolymer composites. Finally, the model is applied to investigate the influence of porosity, processing, and chemistry on the inelastic behavior of geopolymer composites.

2. Theory

2.1. Multiscale conceptual model of geopolymer composites

Our objective is to formulate the effective constitutive behavior of geopolymer composites and connect the behavior to the structure at multiple lengthscales using the framework of rate-independent elasto-plasticity. The first step consists in idealizing the structure at different length-scales. Fig. 1 displays our physics-based idealized model of geopolymer composites with 4 levels of hierarchy. Each level of hierarchy is characterized by a length-scale, a composition, and a specific microstructure. The constitutive behavior is described using linear elasticity and plasticity. Linear elasticity dictates a stress-strain law of the form $\boldsymbol{\sigma} = \mathbb{C}: \boldsymbol{\varepsilon}$, where $\boldsymbol{\sigma}$ is the stress tensor, $\boldsymbol{\varepsilon}$ is the strain tensor, and $\mathbb{C}$ is the fourth-order elastic stiffness tensor [17,18]. Moreover, plasticity is described by a yield criterion of the form $f(\boldsymbol{\sigma}) = 0$ [19,20]. This yield criterion defines a failure envelope. Moreover, the yield criterion is associated with a strength domain, $f(\boldsymbol{\sigma}) \leq 0$, which defines the set of statically admissible stress states. Alternatively, the strength domain can be described via the strain-rate plastic potential $\tilde{W}(\mathbf{d})$ where $\mathbf{d}$ is the strain rate tensor. The stress tensor at the onset of yielding is then given by: $\boldsymbol{\sigma} = \frac{\partial \tilde{W}}{\partial \mathbf{d}}$ [19,20]. The latter definition of the yield criterion and strength domain in terms of plastic potential will enable us to apply variational approaches to compute the effective plastic behavior of a composite material.

Table 1 defines the major mathematical symbols used in this work. In this study, scalars are denoted by italic Roman m or Greek μ letters; vectors by underlined italic letter $\underline{u}$, second-order tensors by boldface italic letters $\mathbf{s}$, and fourth-order tensors by barred letters, $\mathbb{C}$. Moreover, the notation : is employed to denote the double inner tensor product. We recall the fourth-order tensors $\mathbb{J}$ and $\mathbb{K}$ defined by: $\mathbb{J}: \mathbf{A} = \frac{1}{3}\mathrm{Tr}(\mathbf{A})\mathbf{1}$ and $\mathbb{K}: \mathbf{A} = \mathbf{A} - \mathbb{J}: \mathbf{A}$, $\mathrm{Tr}(\mathbf{A}) = \mathbf{1}: \mathbf{A}$ being the trace operator. In particular, $\mathbb{I} = \mathbb{J} + \mathbb{K}$ is the symmetric fourth-order unit tensor whereas $\mathbf{1}$ is the second-order unit tensor.

2.1.1. Level 0

Level 0, angstrom to nanometer level, is the elementary unit: $[SiO_4]$ and $[AlO_4]$ tetrahedra surrounded by alkali monovalent cations for electrical neutrality. At this level, the empirical formula for geopolymer is: $M_n(-(SiO_2)_z - AlO_2)_n \cdot wH_2O$, where M is a monovalent cation (typically, Na^+, K^+, Cs^+), $z = [1,2,3]$, w is the hydration extent and n is the degree of polycondensation [21,22]. The building blocks are $[AlO_4]$ and $[SiO_4]$ tetrahedra. At least three elementary groupings can be distinguished according to the Si:Al atomic ratio: poly(sialate) with Si:Al = 1, poly(sialate-siloxo) with Si:Al = 2, and poly(sialate-disiloxo) with Si:Al = 3.

We build upon the notion of an intrinsic geopolymer skeleton introduced by Smilauer et al. [14]. At level 0, the solid bulk modulus is κ_s and the solid shear modulus is μ_s. Thus, the fourth-order stiffness tensor of the solid skeleton is given by $\mathbb{C}^{(s)} = 3\kappa_s\mathbb{J} + 2\mu_s\mathbb{K}$. Due to the nano-particulate nature, we postulate a strength behavior following the Drucker-Prager yield criterion [23]: $f(\boldsymbol{\sigma}) = \sigma_{eq}/\sqrt{2} + \alpha_s\sigma_m - c_s = 0$ where $\sigma_{eq} = \sqrt{\mathbf{s}: \mathbf{s}}$ is the Mises stress, $\sigma_m = \frac{1}{3}\mathrm{Tr}(\boldsymbol{\sigma})$ is the mean normal stress, and $\mathbf{s} = \boldsymbol{\sigma} - \sigma_m\mathbf{1}$ is the stress deviator. α_s is the internal friction coefficient of the basic geopolymer skeleton whereas c_s is the elemental cohesion.

2.1.2. Level I

Level I, nanometer to submicron level, is the scale of pure geopolymer precursor. The amorphous aluminosilicate gel consists of nanoparticles, 5–40 nm in diameter, separated by nanopores [9,24]. The size of the nano-pores is 3–50 nm and the nanoporosity ϕ ranges from 20 to 40% [24–26]. The elastic constants at level I are the bulk modulus $\kappa^{(I)}$ and the shear modulus $\mu^{(I)}$. We seek to determine the linear upscaling functions $\mathscr{K}^{(I)}$ and $\mathscr{M}(I)$ defined by:

$$\kappa^{(I)} = \mu_s \mathscr{K}^{(I)}\left(\phi, \frac{\kappa_s}{\mu_s}\right); \mu^{(I)} = \mu_s \mathscr{M}^{(I)}\left(\phi, \frac{\kappa_s}{\mu_s}\right) \tag{1}$$

Furthermore, we seek to determine the effective yield criterion at level I: $f^{(I)}(\boldsymbol{\sigma}) = 0$.

2.1.3. Level II

At level II, the material consists of the nanoporous geopolymer precursor (GP) matrix along with inclusions, micropores, and potentially non-reacted phases. The presence of unreacted phases correlates with the use of natural aluminosilicate sources. The unreacted aluminosilicate particles can be eliminated via the use of a synthetic aluminosilicate source [27]. In this work, we assume that non-reacted phases such as non-reacted solid aluminosilicate sources are non-existent. The inclusions usually consists of particles, grains, or fibers. φ is the microporosity, η_2 is the volume fraction of inclusions, and $\eta_I = 1 - \varphi - \eta_2$ is the solid packing density of the nanoporous amorphous geopolymer matrix. Moreover, the inclusion phase is characterized by a bulk modulus κ_2 and a shear modulus μ_2. We seek to calculate the effective bulk and shear moduli at level II, respectively $\kappa^{(II)}$ and $\mu^{(II)}$, which are given by the functionals:

$$\kappa^{(II)} = \mu^{(I)} \mathscr{K}^{(II)}\left(\varphi, \eta_2, \frac{\kappa_I}{\mu_I}\right); \mu^{(II)} = \mu^{(I)} \mathscr{M}^{(II)}\left(\varphi, \eta_2, \frac{\kappa_I}{\mu_I}\right) \tag{2}$$

Herein $\mathscr{K}^{(II)}$ and $\mu^{(II)}$ are the linear upscaling functions at level II. Furthermore, the effective yield criterion at level II is given by $f^{(II)}(\boldsymbol{\sigma}) = 0$.

2.1.4. Level III

Level III, macroscopic scale, is the level of field tests and conventional macroscopic laboratory testing. The structure behaves as a homogeneous medium and the behavior can be appraised via flexural strength tests [28], uniaxial compression tests [29], and tension tests. In the next sections, we employ linear micromechanics to derive the linear upscaling functions at level I and II, and we employ a variational approach based on the linear comparison composite method to derive the yield criterion functions at level I and II.

2.1.5. Dual porosity

Fig. 2 illustrates the dual porosity of metakaolin-based geopolymer matrices. Fig. 2 a) displays a high angle annular dark field Transmitted Electron Microscopy micrograph of potassium geopolymer—of formula $K_2O\ Al_2O_3 4SiO_2 11H_2O$— showing nanopores in the range 50–300 nm [25]. Meanwhile, Fig. 2 b) displays an optical micrograph of potassium geopolymer showing pores in the range 6–600 μm. Gas adsorption tests

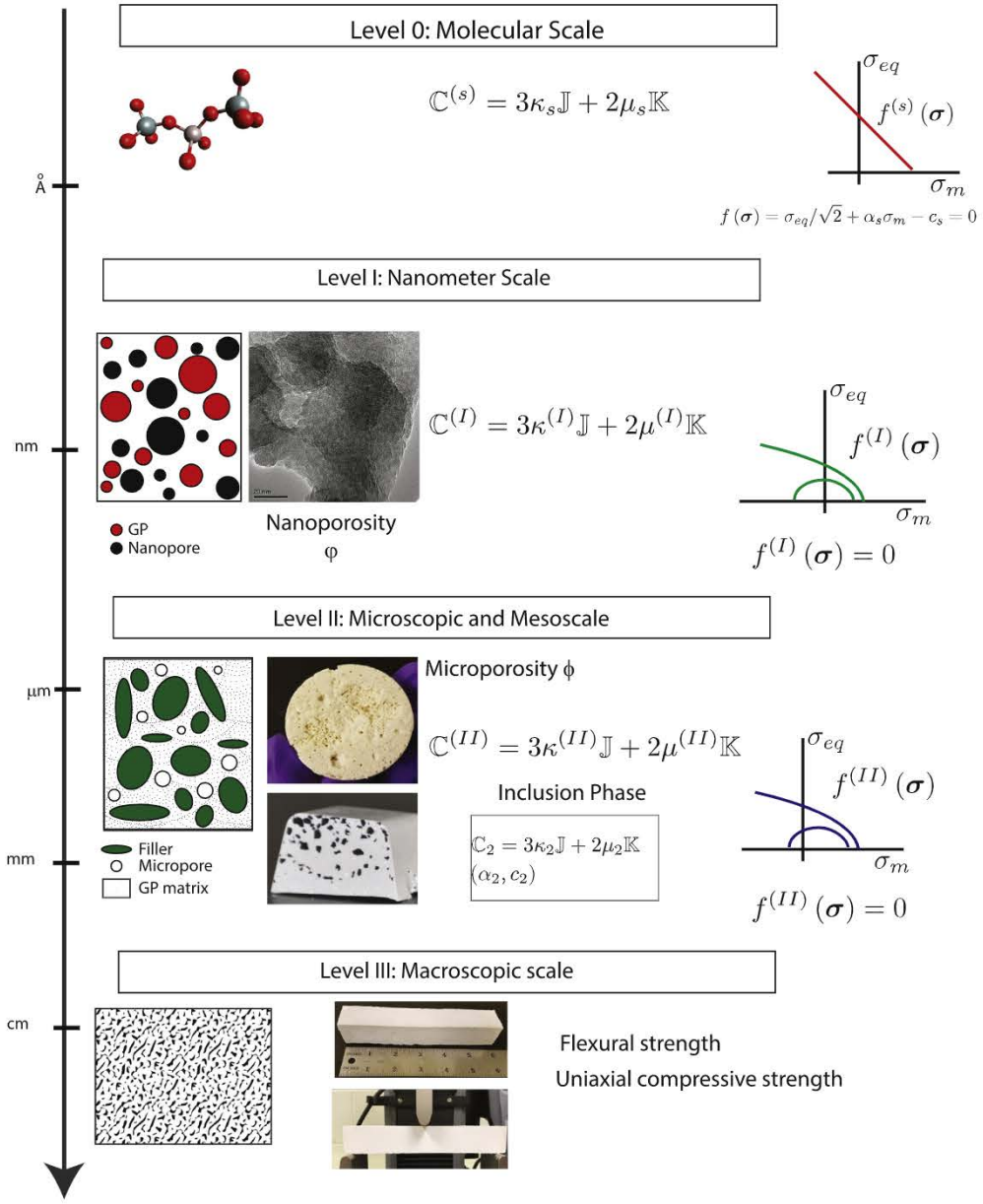

Fig. 1. Multiscale conceptual model for geopolymer composites.

and mercury intrusion porosimetry revealed that the nanoporosity ϕ ranges from 20 to 40% [24–26]. Unlike prior studies that have considered the porosity of geopolymers as a whole, we mark the distinction between nanoporosity and microporosity. In what follows, we will show that the nanoporosity and the microporosity affect the mechanical response in different manners and are themselves controlled by different parameters.

2.2. Linear homogenization

2.2.1. Level I

At level I, the effective stiffness tensor is that of a porous solid, which is given by: $\mathbb{C}^{(I)} = (1-\phi)\mathbb{C}^{(s)}: \mathbb{A}^{(s)}$ [30,31], where ϕ is the porosity at the nanoscale. $\mathbb{A}^{(s)}$ is the strain concentrator tensor for the solid skeleton and is equal to $\mathbb{A}^{(s)} = [(1-\eta_s)(\mathbb{I} - \mathbb{P}_0: \mathbb{C}^{(s)})^{-1} + \eta_s\mathbb{I}]^{-1}$. Herein $\mathbb{P}_0$ is the Hill tensor for a spherical inclusion in an elastic isotropic medium[1] [32]. In particular, assuming the solid to be the reference phase, we can then evaluate the linear upscaling functions at level I, $\mathscr{K}^{(I)}$ and $\mathscr{M}^{(I)}$:

$$\mathscr{K}^{(I)} = (1-\phi)\frac{4\kappa_s}{3\phi\kappa_s + 4\mu_s} \tag{3}$$

$$\mathscr{M}^{(I)} = (1-\phi)\frac{9\kappa_s + 8\mu_s}{(9\kappa_s + 8\mu_s) + (6\kappa_s + 12\mu_s)\phi} \tag{4}$$

2.2.2. Level II

At level II, the inclusion phase is characterized by a volume fraction η_2 and a stiffness tensor $\mathbb{C}_2 = 3\kappa_2\mathbb{J} + 2\mu_2\mathbb{K}$, where κ_2 and μ_2 are respectively the bulk and shear modulus of the inclusions. Denoting by η_I the volume fraction of the geopolymer matrix, the effective stiffness tensor is given by: $\mathbb{C}^{(II)} = \eta_I\mathbb{C}^{(I)}: \mathbb{A}^{(I)} + \eta_2\mathbb{C}_2: \mathbb{A}_2$ [30,31]. $\mathbb{A}^{(I)}$ is the strain concentration tensor of the geopolymer matrix, $\mathbb{A}^{(2)}$ is the strain concentration tensor of the inclusion or filler phase and $\varphi = 1 - \eta_I - \eta_2$ is the volume content of micropores. If we consider the geopolymer matrix—phase (I)—as the reference phase and if we take into account

[1] In particular, $\mathbb{P}_0$ is given by $\mathbb{P}_0 = \frac{1}{3\kappa^0 + 4\mu^0}\mathbb{J} + \frac{3}{5\mu^0}\frac{\kappa^0 + 2\mu^0}{3\kappa^0 + 4\mu^0}\mathbb{K}$ where κ^0 and μ^0 are

Table 1
Description of the mathematical symbols used in this study.

Symbol	Physical Meaning
α_s	internal friction coefficient of solid skeleton at level 0
$A^{(n)}$	short axis of failure envelope at level n
$\widetilde{\mathbb{A}^{(i)}}$	dilute strain concentration tensor of phase i
$\mathbb{A}^{(i)}$	strain concentration tensor of phase i
$B^{(n)}$	long axis of failure envelope at level n
$\mathbb{C}^{(i)}$	stiffness tensor of phase i
c_s	cohesion of solid skeleton at level 0
$\mathbf{d}$	strain rate tensor
d_m	volumetric strain rate
d_{eq}	norm of the deviatoric strain rate tensor
$\boldsymbol{\delta}$	deviatoric strain rate tensor
$\boldsymbol{\varepsilon}$	strain tensor
$\kappa^{(i)}$	bulk modulus of phase i
$\mathscr{K}^{(n)}$	linear upscaling function for the bulk modulus at level n
$\mu^{(i)}$	shear modulus of phase i
$\mathscr{M}^{(n)}$	linear upscaling function for the shear modulus at level n
$S_0^{(i)}$	offset of failure envelope at level n
η_i	volume fraction of phase i
P	Total porosity
$\boldsymbol{\sigma}$	stress tensor
$\mathbf{s}$	deviatoric stress tensor
σ_{eq}	Mises stress
σ_m	Mean normal stress
τ	hydrostatic eigenstress
$V^{(I)}$	nonlinearity measure function for phase i
$w^{(I)}$	nonlinear plastic potential for phase i
$w_L^{(i)}$	quadratic energy density for phase i
$\tilde{W}_0^{(n)}$	effective elastic strain rate energy at level n
$\tilde{W}^{(n)}$	effective plastic potential at level n

the interaction between particles, we can write the expression of the dilute strain concentration tensors $\widetilde{\mathbb{A}^{(0)}}$, $\widetilde{\mathbb{A}^{(I)}}$, and $\widetilde{\mathbb{A}^{(2)}}$ defined respectively for the micropore phase, geopolymer matrix phase, and inclusion phase:

$$\widetilde{\mathbb{A}^{(0)}} = (\mathbb{I} - \mathbb{P}_I : \mathbb{C}^{(I)})^{-1}; \quad \widetilde{\mathbb{A}^{(I)}} = \mathbb{I}; \quad \widetilde{\mathbb{A}_2} = \left(\mathbb{I} + \mathbb{P}_I : \left(\mathbb{C}_2 - \mathbb{C}^{(I)}\right)\right)^{-1} \tag{5}$$

The strain concentration tensors for respectively the geopolymer matrix phase, $\mathbb{A}^{(I)}$ and the inclusion phase, $\mathbb{A}_2$, are then given by:

$$\mathbb{A}^{(I)} = [\varphi\, \widetilde{\mathbb{A}^{(0)}} + \eta_I\, \widetilde{\mathbb{A}^{(I)}} + \eta_2\, \widetilde{\mathbb{A}_2}]^{-1} \tag{6}$$

$$\mathbb{A}_2 = \widetilde{\mathbb{A}_2} : [\varphi\, \widetilde{\mathbb{A}^{(0)}} + \eta_I\, \widetilde{\mathbb{A}^{(I)}} + \eta_2\, \widetilde{\mathbb{A}_2}]^{-1} \tag{7}$$

with $\mathbb{P}_I = \frac{1}{3\kappa^{(I)} + 4\mu^{(I)}}\mathbb{J} + \frac{3}{5\mu^{(I)}}\frac{\kappa^{(I)} + 2\mu^{(I)}}{3\kappa^{(I)} + 4\mu^{(I)}}\mathbb{K}$ being the Hill tensor for a spherical inclusion embedded in medium (I)—the nanoporous geopolymer matrix. We can then derive the expression of the linear upscaling functions at level II, respectively $\mathscr{K}^{(II)}$ and $\mathscr{M}^{(II)}$.

2.3. Strength criteria

Our objective is to understand the sources of energy dissipation within geopolymer composites. In the elastic range, no energy dissipation occurs and the material volume elements sustain the applied load through elastic deformations, stretching and rotating. In the inelastic range, energy dissipation occurs through three primary mechanisms: volume changes of free volume elements or pores, irreversible deformations of solid elements, and friction between grains. Free volume elements are characterized by the porosity that we divide in nanoporosity, ϕ, and microporosity, φ, depending on the pore size. The irreversible deformation of solid elements is characterized via the cohesion c. Finally, the friction between grains is characterized via the coefficient of internal friction α.

We focus on the definition of the strength domain as bounded by a yield curve of equation $f(\boldsymbol{\sigma}) = 0$ [19,20]. The region $f(\boldsymbol{\sigma}) = 0$ then defines the region of stress states that are statically admissible and can be sustained by the material. We focus on a set of convex yield criteria that are cohesive frictionless and cohesive frictional. Table 2 lists the main types of yield criterion considered. Fig. 3 shows the corresponding strength domains. Cohesive frictionless behaviors are characterized by a symmetry of behavior in tension and compression. The standard cohesive frictionless criterion is the Von Mises criterion: $\sigma_{eq}/\sqrt{2} - c = 0$. The Von Mises yield criterion is characteristic of metals and some polymeric materials. In contrast, cohesive frictional materials are characterized by an asymmetry of behavior in tension and compression. The Drucker-Prager criterion, $\frac{\sigma eq}{\sqrt{2}} + \alpha_2\sigma_m - c_2 = 0$, is a pressure-dependent criterion that is typical of soils, rocks, and concrete. The Drucker-Prager criterion is characterized by a cohesion c and a friction coefficient, α. Finally, we consider two families of extended Drucker-Prager criteria: hyperbolic and elliptical. The hyperbolic yield stress criterion is often used to provide a smooth approximation of the Drucker-Prager criterion and is typical of clay-bearing rocks. Finally, the elliptical yield criterion is often used to model high-porosity rocks [33].

The yield criterion can be used to estimate the strength in tension or compression. Given a uniaxial tension test of uniaxial stress σ_y, the mean normal stress is equal to $\sigma_m = \sigma_y/3$ and the Mises stress is given by $\sigma_{eq} = \frac{\sqrt{6}}{3}|\sigma_y|$. The uniaxial tensile strength is then computed as the

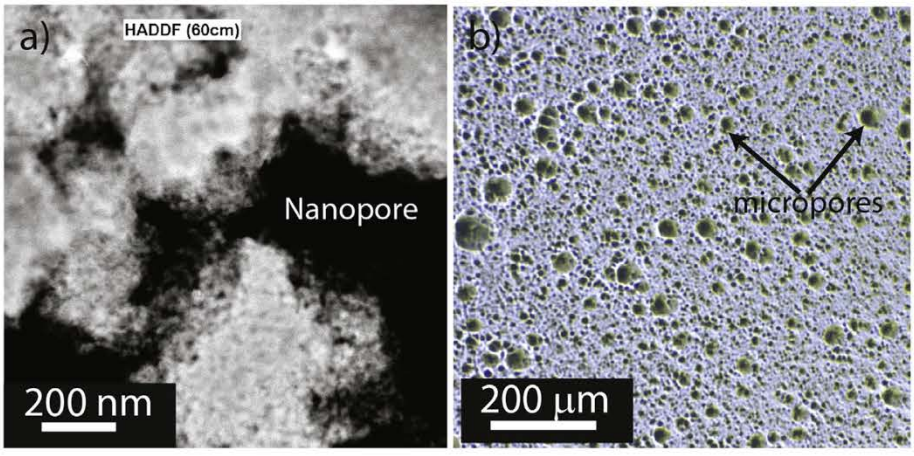

Fig. 2. Dual porosity of pure metakaolin-based potassium-geopolymer. a) Transmitted Electron Microscopy micrograph. Source [25]. b) Optical micrograph.

Table 2
Main yield criteria considered in this study. σ_{eq} is the Mises stress whereas σ_m is the mean normal stress.

Criterion	Yield function $f(\sigma) = 0$	Nature
Von Mises	$\frac{\sigma_{eq}}{\sqrt{2}} - c = 0$	frictionless
Drucker-Prager	$\frac{\sigma_{eq}}{\sqrt{2}} + \alpha\sigma_m - c = 0$	frictional
Hyperbolic	$(\sigma_m - S)^2 - \frac{A^2}{2B^2}\sigma_{eq}^2 - A^2 = 0$	frictional
Elliptical	$(\sigma_m - S)^2 + \frac{A^2}{2B^2}\sigma_{eq}^2 - A^2 = 0$	frictional

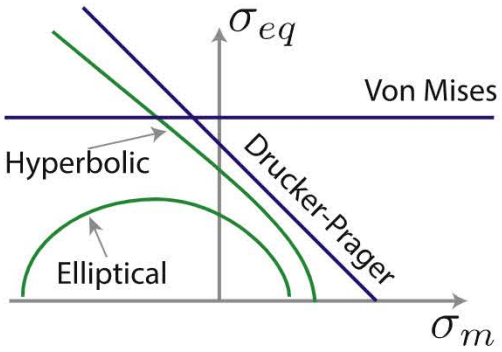

Fig. 3. Schematic representation of the different yield criteria considered in this study.

positive root of the equation $f^{(II)}(\sigma_{eq}, \sigma_m) = 0$. For instance, for a Von Mises type material, the uniaxial tensile strength, UTS, is linked to the cohesion via: $UTS = c\sqrt{3}$. Meanwhile, for a Drucker-Prager type material, the uniaxial tensile strength is linked to the cohesion c and the friction coefficient α via: $UTS = 3c/(\sqrt{3} + \alpha)$ [34].

2.3.1. Talbot & willis variational approach

In order to upscale the strength behavior of geopolymer composites, we formulate novel solutions based on the variational approach pioneered by Talbot, Willis, and Castaneda [35–37]. Starting from the principle of minimum potential energy, the basic idea is to extend the Hashin-Sthrikman variational framework to nonlinear composites. In other words, we place ourselves in the plastic regime where the material has exhausted its ability to store mechanical energy through reversible deformations and we estimate the maximum energy dissipation potential based on a comparison composite medium. The method has been successfully applied to represent the nonlinear response of metal composites [38], elastomers [39], cementitious materials [40,41], and geomaterials [42,43]. However, due to the high friction coefficient values of the solid skeleton at the nanoscale, prior solutions are inapplicable to geopolymer composites and new solutions must be formulated: the latter is our objective.

2.3.2. Level 0

At level 0, the solid skeleton is characterized by a plane strain modulus m_s, a Poisson's ratio ν_s, a cohesion c_s, and an internal friction coefficient α_s. In particular, the friction α_s is decoupled from the Poisson's ratio ν_s. Given the strain rate tensor $\mathbf{d} = \frac{1}{3}d_m\mathbf{1} + \boldsymbol{\delta}$, we can express the solid homogeneous quadratic energy density: $w_L^{(s)}(\mathbf{d}) = \frac{1}{2}\kappa_s d_m^2 + \mu_s d_{eq}$—with $d_{eq} = \sqrt{\boldsymbol{\delta}:\boldsymbol{\delta}}$. d_m is the volumetric strain rate whereas $\boldsymbol{\delta}$ is the deviator strain rate tensor. Then, we compute the nonlinearity measure, $V^{(s)}$, which measures the nonlinearity in the potential of the solid. $V^{(s)}$ is given by

$$V^{(s)} = \sup_{\mathbf{d},\tau}\{w^{(s)}(\mathbf{d}) - w_L^{(s)}(\mathbf{d}) - \tau:\mathbf{d}\} \tag{8}$$

Herein $w^{(s)}(\boldsymbol{\varepsilon})$ is the nonlinear plastic potential function and $\tau = \tau\mathbf{1}$ is the hydrostatic eigenstress due to thermal strains. k_s is the geopolymer skeleton bulk modulus and μ_s is the geopolymer skeleton shear modulus. In particular, for a Drucker-prager material, after replacing the supremum with a stationary estimate, we calculate the following expression of $V^{(s)}$:

$$V^{(s)} = \frac{1}{2\mu_s}\frac{1}{\zeta_0}\left(\frac{c_s}{\alpha_s} - \tau\right)^2 \tag{9}$$

with $\zeta_0 = \frac{\kappa_s}{\mu_s} + \frac{1}{\alpha_s^2}$.

2.3.3. Level I

At level I, the composite consists of the solid skeleton and nanopores of volume fraction ϕ. The effective elastic strain rate energy $\tilde{W}_0^{(I)}$ includes a quadratic term in the effective strain rate $\mathbf{d} = \frac{1}{3}d_m\mathbf{1} + \boldsymbol{\delta}$, a linear term in the prestress, τ, and a quadratic term in the prestress:

$$\tilde{W}_0^{(I)} = \frac{1}{2}\kappa^{(I)}d_m^2 + \mu^{(I)}d_{eq}^2 + \beta^{(I)}\tau d_m - \frac{\gamma^{(I)}}{2}\frac{\tau^2}{\mu_s} \tag{10}$$

with $d_{eq} = \sqrt{\boldsymbol{\delta}:\boldsymbol{\delta}}$ and

$$\beta^{(I)} = \frac{\kappa^{(I)}}{\kappa_s}; \quad \gamma^{(I)} = \xi\frac{\mu_s}{\kappa_s}\left(1 - \phi - \frac{\kappa^{(I)}}{\kappa_s}\right) \tag{11}$$

τ is the prestress due to thermal strains. ξ is used to adjust the influence of the quadratic term in the prestress on the mechanical behavior. For $\xi = 0$ the quadratic term is negligible, whereas for $\xi = 1$, the quadratic term is significant.

$\kappa^{(1)}$—respectively $\mu^{(1)}$—is the effective bulk—respectively shear—-modulus at level I, which is given by Eq. (3) —respectively Eq. (4). An upper bound for the effective potential at level I, $\tilde{W}(\mathbf{d})$ is given by:

$$\tilde{W}(\mathbf{d}) \leq \inf_{\mu_s,\kappa_s,\tau}\{\tilde{W}_0^{(I)} + (1-\phi)V_s\} \tag{12}$$

Replacing the infimum by a stationary estimate, and considering linear comparison composites for which the Poisson's ratio of the solid phase is equal to ν_s, we obtain two stationary conditions:

$$\frac{\partial}{\partial\mu_s}(\tilde{W}_0^{(I)} + (1-\phi)V_s) = 0 \tag{13}$$

$$\frac{\partial}{\partial\tau}(\tilde{W}_0^{(I)} + (1-\phi)V_s) = 0 \tag{14}$$

The strategy consists in finding the stationary point (τ^*, μ^*) solution of Eqs. (13) and (14) and replacing τ^* and μ^* by their values in $\tilde{W}_0^{(I)} + \eta_s V_s$. Following these steps, we can write the variational estimate of the effective potential as:

$$\tilde{W}^{(I)}(\mathbf{d}) = S_0^{(I)}d_m + \mathrm{sgn}(\chi^{(I)})\sqrt{A^{(I)^2}d_m^2 + 2\,\mathrm{sgn}(\chi^{(I)})B^{(I)^2}d_{eq}^2} \tag{15}$$

where the quantities $(\chi^{(I)}, S_0^{(I)}, A^{(I)}, B^{(I)})$ are defined as:

$$\chi^{(I)} = \mathscr{K}^{(I)} + \frac{\beta^{(I)^2}}{\gamma^{(I)} - \frac{1-\phi}{\zeta_0}} \tag{16}$$

$$S_0^{(I)} = -\frac{c_s}{\alpha_s}\frac{1-\phi}{\zeta_0}\frac{\beta^{(I)}}{\gamma^{(I)} - \frac{1-\phi}{\zeta_0}} \tag{17}$$

$$A^{(I)} = \frac{c_s}{\alpha_s}\sqrt{\frac{\gamma^{(I)}\frac{1-\phi}{\zeta_0}}{\gamma^{(I)} - \frac{1-\phi}{\zeta_0}}\chi^{(I)}} \tag{18}$$

$$B^{(I)} = \frac{c_s}{\alpha_s}\sqrt{\frac{\gamma^{(I)}\frac{1-\phi}{\zeta_0}}{\left|\gamma^{(I)} - \frac{1-\phi}{\zeta_0}\right|}}\sqrt{\mathscr{M}^{(\mathscr{I})}} \tag{19}$$

Herein $\mathrm{sgn}(\chi^{(I)})$ denotes the sign function equal to 1 if $\chi^{(I)} > 0$ and

equal to -1 if $\chi^{(I)} < 0$. Upon yielding, the stress tensor $\boldsymbol{\sigma} = \sigma_m 1 + \mathbf{s}$ obeys the normality rule: $\boldsymbol{\sigma} = \frac{\partial \tilde{W}(\mathbf{d})}{\partial \mathbf{d}}$.[2] In particular, $\boldsymbol{\sigma}$ obeys the effective failure criterion:

$$f^{(I)}(\boldsymbol{\sigma}) = (\sigma_m - S_0^{(I)})^2 + \text{sgn}(\chi^{(I)})\left(\frac{A^{(I)}}{B^{(I)}}\frac{\sigma_{eq}}{\sqrt{2}}\right)^2 = (A^{(I)})^2 \tag{20}$$

For $\chi < 0$, the failure envelope described by Eq. (20) is a hyperbole. Whereas for $\chi > 0$, the failure envelope is an ellipse. For $\chi = 0$, the failure envelope degenerates into a parabola. In the asymptotic case of a matrix-pore morphology with a low value of the nanoporosity ϕ, the failure criterion at level I is a Drucker-Prager criterion.

2.3.4. Level II: pure geopolymer

Fig. 4 displays the structural model of pure geopolymer. At level II, pure and unreinforced geopolymer consists of a nanoporous geopolymer phase of packing density η_I along with micropores of volume fraction $\varphi = 1 - \eta_I$. The nonlinearity measure function for the nanoporous geopolymer phase is given by:

$$V^{(I)} = \frac{1}{2}\frac{1}{\mu^{(I)}}\frac{(S_0^{(I)} - \tau_I)^2}{\zeta} + \frac{\text{sgn}(\chi^{(I)})}{2}\frac{B^{(I)2}}{\mu^{(I)}} \tag{21}$$

The macroscopic elastic strain rate energy at level II reads as:

$$\tilde{W}_0^{(II)} = \frac{1}{2}\kappa^{(II)} d_m^2 + \mu^{(II)} d_{eq}^2 + \beta^{(II)}\tau_I d_m - \frac{\gamma^{(II)}}{2}\frac{\tau_I^2}{\mu_I} \tag{22}$$

where τ_I is the prestress in the nanoporous geopolymer matrix and $\beta^{(II)}$ and $\gamma^{(II)}$ are functions of ν_s, m_s, ϕ, and φ and they are defined as:

$$\beta^{(II)} = \frac{\kappa^{(II)}}{\kappa^{(I)}} \tag{23}$$

$$\gamma^{(II)} = \frac{\mu^{(I)}}{\kappa^{(I)}}\left(\eta_I - \frac{\kappa^{(II)}}{\kappa^{(I)}}\right) \tag{24}$$

An upper bound for the effective potential at level II then reads:

$$\tilde{W}^{(II)} \leq \tilde{W}_0^{(II)} + \eta_I V^{(I)} \tag{25}$$

Using similar steps as previously explained, the effective potential at level II for pure geopolymer can then be written as:

$$\tilde{W}^{(II)}(\mathbf{d}) = S_0^{(II)} d_m + \text{sgn}(\chi^{(II)})\sqrt{A^{(II)^2} d_m^2 + 2\,\text{sgn}(\chi^{(II)}) B^{(II)^2} d_{eq}^2} \tag{26}$$

$\chi^{(II)}$ determines the shape of the failure envelope, whereas $S_0^{(II)}$, $A^{(II)}$, and $B^{(II)}$ are respectively the offset, short axis and long axis of the failure envelope. The quantities ($\chi^{(II)}$, $S_0^{(II)}$, $A^{(II)}$, $B^{(II)}$) are defined as:

$$\chi^{(II)} = \mathscr{M}^{(II)} + \frac{\beta^{(II)2}}{\gamma^{(II)} - \frac{\eta_I}{\zeta}} \tag{27}$$

$$S_0^{(II)} = -\frac{\frac{\eta_I}{\zeta}\beta^{(II)}}{\gamma^{(II)} - \frac{\eta_I}{\zeta}} S_0^{(I)} \tag{28}$$

$$A^{(II)} = \sqrt{\frac{\gamma^{(II)}\frac{\eta_I}{\zeta}}{\gamma^{(II)} - \frac{\eta_I}{\zeta}} S_0^{(I)2} + \eta_I \text{sgn}(\chi^{(II)}) B^{(I)2}} \times \sqrt{|\chi^{(II)}|} \tag{29}$$

[2] Using the normality rule and the decomposition of the stress tensor into spherical and deviatoric components, $\boldsymbol{\sigma} = \sigma_m 1 + \mathbf{s}$, we can connect the mean normal stress σ_m to the volumetric strain rate d_m; we can also connect the Mises stress σ_{eq} to the norm of the deviatoric strain rate tensor d_{eq}. Using the chain rule, we have: $\frac{\partial \tilde{W}(\mathbf{d})}{\partial \mathbf{d}} = \frac{\partial \tilde{W}}{\partial d_m}\frac{\partial d_m}{\partial \mathbf{d}} + \frac{\partial \tilde{W}}{\partial d_{eq}}\frac{\partial deq}{\partial \mathbf{d}}$. Moreover, $\frac{\partial d_m}{\partial \mathbf{d}} = 1$ whereas $\frac{\partial d_{eq}}{\partial \mathbf{d}} = \frac{\delta}{d_{eq}}$. Thus.$\boldsymbol{\sigma} = \frac{\partial \tilde{W}}{\partial \mathbf{d}} = \frac{\partial \tilde{W}}{\partial d_m}1 + \frac{\partial \tilde{W}}{\partial d_{eq}}\frac{\delta}{d_{eq}} = \sigma_m 1 + \mathbf{s}$Thus, we can conclude: $\sigma_m = \frac{\partial \tilde{W}}{d_m}$; $\sigma_{eq}^2 = \left(\frac{\partial \tilde{W}}{\partial d_{eq}}\right)^2$

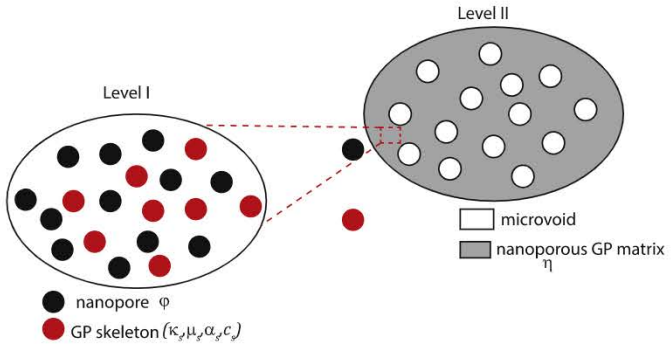

Fig. 4. Multiscale conceptual model for pure and unreinforced geopolymer.

$$B^{(II)} = \sqrt{\frac{\gamma^{(II)}\frac{\eta_I}{\zeta}}{\gamma^{(II)} - \frac{\eta_I}{\zeta}} S_0^{(I)2} + \eta_I \text{sgn}(\chi^{(II)}) B^{(I)2}} \times \sqrt{\mathscr{M}^{(II)}} \tag{30}$$

The failure envelope is elliptical if $\chi^{(II)} > 0$ and it is hyperbolic if $\chi^{(II)} < 0$. The equation of the failure envelope is given by:

$$f^{(II)}(\boldsymbol{\sigma}) = (\sigma_m - S_0^{(II)})^2 + \text{sgn}(\chi^{(II)})\left(\frac{\sigma_{eq}}{\sqrt{2}}\frac{A^{(II)}}{B^{(II)}}\right)^2 = (A^{(II)})^2 \tag{32}$$

2.3.5. Level II: geopolymer with cohesive frictionless inclusion phase

We consider a three-phase geopolymer composite at level II as shown in Fig. 1. The second phase is cohesive frictionless. The second phase is characterized by a volume fraction η_2, a bulk modulus κ_2, a shear modulus μ_2, and a cohesion c_2. In turn, the volume fraction of micropores is φ, and the packing density of the nanoporous geopolymer matrix phase is $\eta_I = 1 - \varphi - \eta_2$. Given that the second phase is cohesive frictionless, only the nanoporous matrix phase exhibits a non-zero prestress τ_I. This case is very similar to the case of a microporous pure geopolymer. In particular, the generic expression of the macroscopic elastic strain rate energy $\tilde{W}_0^{(II)}$ is still given by Eq. (22) except that, the functions $\beta^{(II)}$ and $\gamma^{(II)}$ are given by different expressions:

$$\beta^{(II)} = \frac{\kappa^{(II)} - \kappa_2}{\kappa^{(I)} - \kappa_2} \tag{33}$$

$$\gamma^{(II)} = \frac{\mu^{(I)}}{\kappa^{(I)} - \kappa_2}\left(\eta_I - \frac{\kappa^{(II)} - \kappa_2}{\kappa^{(I)} - \kappa_2}\right) \tag{34}$$

Moreover, when calculating the upper bound for the effective potential at level II, we need to account for the nonlinearity measure function for the second phase, $V_2 = \frac{c_2^2}{2\mu_2}$ so that the upper bound is given by:

$$\tilde{W}^{(II)} \leq \tilde{W}_0^{(II)} + \eta_I V^{(I)} + \eta_2 V_2 \tag{35}$$

In order to calculate a stationary estimate of the effective potential at level II, we can use the same steps as in the case of a pure geopolymer. In this case, the generic expression of the effective potential and of the macroscopic failure criterion is the same as Eq. (26) and Eq. (32) except that the actual values of $A^{(II)}$ and $B^{(II)}$ now depend on c_2, the cohesion of the second phase:

$$A^{(II)} = \sqrt{\frac{\gamma^{(II)}\frac{\eta_1}{\zeta}}{\gamma^{(II)} - \frac{\eta_1}{\zeta}} S_0^{(I)2} + \eta_1 \text{sgn}(\chi^{(II)}) B^{(I)2} + \eta_2 \frac{\mu^{(I)}}{\mu_2} c_2^2} \times \sqrt{|\chi^{(II)}|} \tag{36}$$

$$B^{(II)} = \sqrt{\frac{\gamma^{(II)}\frac{\eta_1}{\zeta}}{\gamma^{(II)} - \frac{\eta}{\zeta}} S_0^{(I)2} + \eta_1 \text{sgn}(\chi^{(II)}) B^{(I)2} + \eta_2 \frac{\mu^{(I)}}{\mu_2} c_2^2} \times \sqrt{\mathscr{M}^{(II)}} \tag{37}$$

In other words, compared to the pure microporous geopolymer, the second cohesive frictionless phase influences primarily the short and the second axis of the failure envelope, whereas the offset remains the same.

2.3.6. Level II: geopolymer with cohesive frictional inclusion phase

We now consider the case where the inclusion phase displays a cohesive-frictional plastic yield criterion. For instance, let's assume a hyperbolic yield criterion of the form $f(\boldsymbol{\sigma}) = (\sigma_m - S_2)^2 - \frac{A_2^2}{2B_2^2}\sigma_{eq}^2 - A_2^2 = 0$. We must account for the prestress τ_2 of the second phase which is induced by thermal strains. As a result of the prestress for the cohesive frictional inclusion phase τ_2, the nonlinearity measure function for phase 2 reads $V_2 = \frac{1}{2\mu_2}\frac{(S_2-\tau_2)^2}{\zeta_2} - \frac{B_2^2}{2\mu_2}$, where $\zeta_2 = \frac{\kappa_2}{\mu_2} + \frac{A_2^2}{B_2^2}$, with κ_2 and μ_2 being respectively the bulk modulus and shear modulus for phase 2. Moreover, the expression of the macroscopic elastic strain rate energy involves both τ_2 and τ_I, the prestress for the nanoporous geopolymer matrix:

$$\tilde{W}_0^{(II)} = \frac{1}{2}\varkappa^{(II)} d_m^2 + \mu^{(II)} d_{eq}^2 + \alpha^{(II)}(\tau_I - \tau_2)d_m - \frac{\gamma^{(II)}}{2}\frac{(\tau_I - \tau_2)^2}{\mu_I} \tag{38}$$

Furthermore, the prestresss τ_2 also appears in the nonlinearity function of phase 2. Thus in order to approximate $\tilde{W}^{(II)}$, we need to find the stationary value of the quantity:

$$\tilde{W}^{(II)} = \text{stat}_{\mu_1,\tau_I,\tau_2}\tilde{W}_0^{(II)} + \eta_I V^{(I)} + \eta_2 V_2 \tag{39}$$

Thus, there are three stationarity equations to solve:

$$\frac{\partial \tilde{W}^{(II)}}{\partial \tau_I} = 0 \tag{40}$$

$$\frac{\partial \tilde{W}^{(II)}}{\partial \tau_2} = 0 \tag{41}$$

$$\frac{\partial \tilde{W}^{(II)}}{\partial \mu_I} = 0 \tag{42}$$

Eqs. (40) and (41) lead to a linear system of the second order in (τ_I^*, τ_2^*). After solving this system, we obtain the optimal values of the prestress for both the nanoporous geopolymer matrix and the inclusion phase:

$$\tau_I^* = \frac{\beta^{(II)} d_m \frac{\widetilde{\eta_2}}{\zeta_2}\mu_I^* + \left(\gamma^{(II)} - \frac{\widetilde{\eta_2}}{\zeta_2}\right)\frac{\eta_I}{\zeta}S_0^{(I)} + \gamma^{(II)}\frac{\widetilde{\eta_2}}{\zeta_2}S_2}{\Delta} \tag{44}$$

$$\tau_2^* = \frac{-\beta^{(II)}\frac{\eta_I}{\zeta}\mu_I^* + \gamma^{(II)}\frac{\widetilde{\eta_2}}{\zeta}S_0^{(I)} + \left(\gamma^{(II)} - \frac{\eta_I}{\zeta}\right)\frac{\widetilde{\eta_2}}{\zeta_2}S_2}{\Delta} \tag{45}$$

where $\widetilde{\eta_2} = \eta_2\frac{\mu^I}{\mu_2}$ and $\Delta = \gamma^{(I)}\left(\frac{\eta_I}{\zeta} + \frac{\widetilde{\eta_2}}{\zeta_2}\right) - \frac{\eta_I}{\zeta}\frac{\widetilde{\eta_2}}{\zeta_2}$. After replacing τ_I^* and τ_2^* by their respective values in Eq. (42), we can solve for μ_I^*:

$$\left[\left(\mathscr{K}^{(II)} + \beta^{(II)2}\frac{\frac{\eta_I}{\zeta} + \frac{\widetilde{\eta_2}}{\zeta_2}}{\Delta}\right)d_m^2 + 2\mathscr{M}^{(II)}d_{eq}^2\right]\mu_I^{*2} = \gamma^{(II)}\frac{\frac{\eta_I}{\zeta}\frac{\widetilde{\eta_2}}{\zeta_2}}{\Delta}\left(S_0^{(I)} - \frac{c_2}{\alpha_2}\right)^2 + \eta_I \text{sgn}(\chi^{(II)})B^{(I)2} \tag{46}$$

Thus, the macroscopic failure criterion is still of the form Eq. (32), with the expressions of $\chi^{(II)}$, $A^{(II)}$, $B^{(II)}$, and $S_0^{(II)}$ given by:

$$\chi^{(II)} = \mathscr{K}^{(II)} + \beta^{(II)2}\frac{\frac{\eta_I}{\zeta} + \frac{\widetilde{\eta_2}}{\zeta_2}}{\Delta} \tag{47}$$

$$S_0^{(II)} = -(S_0^{(I)} - S_2)\frac{\frac{\eta_I}{\zeta}\frac{\widetilde{\eta_2}}{\zeta_2}}{\Delta}\alpha^{(II)} \tag{48}$$

$$A^{(II)} = \sqrt{\gamma^{(II)}\frac{\frac{\eta_I}{\zeta}\frac{\widetilde{\eta_2}}{\zeta_2}}{\Delta}(S_0^{(I)} - S_2)^2 + \eta_I \text{sgn}(\chi^{(II)})B^{(I)2} - \widetilde{\eta_2}B_2^2}}{\sqrt{|\chi^{(II)}|}} \tag{49}$$

$$B^{(II)} = \sqrt{\gamma^{(II)}\frac{\frac{\eta_I}{\zeta}\frac{\widetilde{\eta_2}}{\zeta_2}}{\Delta}(S_0^{(I)} - S_2)^2 + \eta_I \text{sgn}(\chi^{(II)})B^{(I)2} - \widetilde{\eta_2}B_2^2}}{\sqrt{|\mathscr{M}^{(II)}|}} \tag{50}$$

The macroscopic uniaxial compressive strength UCS and the macroscopic uniaxial tensile strength UTS are then solutions of the equation:

$$\left[\frac{1}{9} + \text{sgn}(\chi^{(II)})\left(\frac{A^{(II)}}{B^{(II)}}\right)^2\right]x^2 - \frac{2}{3}S_0^{(II)}x + (S_0^{(II)})^2 - (A^{(II)})^2 = 0 \tag{51}$$

There are striking differences between the addition of a cohesive frictionless phase and the addition of a cohesive frictional phase. Unlike a cohesive frictionless phase, for a cohesive frictional phase, the internal friction angle of the filler phase will influence the shape (ellipse, parabola, or hyperbola) of the macroscopic failure envelope. Another difference is that the offset of the macroscopic failure envelope depends on the elasto-plastic characteristics of the filler phase. Nevertheless, for both a cohesive frictionless and a cohesive frictional phase, the long and short axis of the macroscopic failure envelope are influenced by the cohesion of the inclusion phase.

In the next sections, we calibrate our model on pure geopolymer and then validate the theory on fiber-reinforced and particulate geopolymer composites. We then explore the influence of mix design and chemistry on the failure envelope of geopolymer composites.

3. Results

3.1. Calibration of the constitutive parameters for unreinforced potassium geopolymer

Most experimental studies on pure geopolymer have focused at the macroscopic scale, thereby probing a composite response. Herein, we seek to evaluate the intrinsic constants of the geopolymer skeleton at the molecular level, $(m_s, \nu_s, c_s, \alpha_s)$. To this end, nanoindentation tests were performed on pure geopolymer samples with chemical formula $K_2O\ Al_2O_3 4SiO_2 11H_2O$. The synthesis procedure is summarized here. First, a silicate solution was prepared by dissolving amorphous silica in a solution of potassium hydroxide. After 24 h, calcined metakaolin MK750 was mixed into the silicate solution using an IKA overhead stirrer and then a Thinky ARE 310 planetary centrifugal mixer. After deaeration in the centrifugal mixer, the resulting slurry was then poured into cylindrical molds. The molds were vibrated using a vibrating table to release residual macroscopic air bubbles and allowed to cure at a temperature of 22°C for 21 days.

Nanoindentation tests were carried out using an Anton Paar nanohardness tester equipped with a Berkovich indenter. Prior to testing, the area function for the Berkovich probe was calibrated using fused silica as a reference material. A 20×20 indentation grid was carried out. During each test, the vertical force was progressively increased until a maximum value of 5 mN, held constant for 5 s and then the probe was carefully removed. For all tests, the loading/unloading phase lasted 30 s. For each test i, the indentation modulus M_i and indentation hardness H_i were calculated following the Oliver & Pharr method [45].

The intrinsic characteristics of the geopolymer skeleton at level 0 along with the local microporosity values at level II were computed using a constrained optimization algorithm so as to be able to reproduce the experimental nanoindentation measurements. The objective was to minimize the quantity:

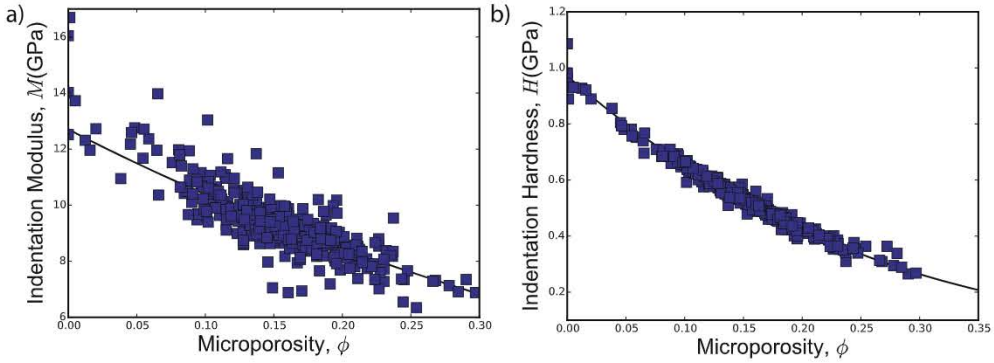

Fig. 5. Model validation on unreinforced potassium MK750 geopolymer. The blue dots represent the experimental values of the indentation modulus M and indentation hardness H from a 20×20 indentation grid carried out on potassium geopolymer. The solid lines represent the theoretical function for the indentation modulus and hardness; those theoretical functions were computed by implementing our constitutive model into a finite element simulation of indentation testing. (For interpretation of the references to colour in this figure legend, the reader is referred to the Web version of this article.)

$$\min_{m_s,c_s,\alpha_s,\varphi_i}\left(\frac{M_i - M(m_s,\nu_s,\phi,\varphi_i)}{M_0}\right)^2 + \left(\frac{H_i - H(\nu_s,c_s,\alpha_s,\phi,\varphi_i)}{H_0}\right)^2 \quad (52)$$

Herein m_s is the plane strain modulus of the skeleton at level 0, ν_s is the Poisson's ratio, α_s is the friction angle, and c_s is the cohesion. The nanoporosity of the potassium geopolymer matrix was set at $\phi = 0.4$ based on gas physical absorption tests carried out by Kriven and coworkers on unreinforced geopolymer samples [24,25]. The theoretical indentation functions were calculated using a numerical finite element model which is detailed in Ref. [46]. The purpose of the finite element model is to simulate indentation testing with a conical probe into a material whose constitutive law at the mesoscale is given by the theoretical linear upscaling functions in Eq. (2) and the theoretical yield functions given in Eq. (32). The resulting penetration depth-force curves were then analyzed so as to extract the theoretical value of the indentation hardness and indentation modulus.

Fig. 5 compares the experimental data and the theoretical predictions for both the indentation hardness and the indentation modulus. A good agreement is observed with a relative error of 5.0% for the indentation modulus and 2.1% for the indentation hardness. The computed characteristics of the geopolymer skeleton at the molecular level (level 0) are: $m_s = 29.77$ GPa, $c_s = 18.00$ GPa, $\alpha_s = 0.76$, and $\nu_s = 0.22$.

Fig. 6 investigates the influence of the microporosity on the failure behavior of unreinforced postassium-based MK750 geopolymer. Fig. 6 a) displays the indentation curves corresponding to different local microporosity levels. As the microporosity φ increases, the material becomes softer and more compliant. As φ increases from 8% to 21%, the penetration depth increases from 632 nm to 810 nm. The increase in penetration depth is followed by a decrease in the indentation modulus from 11.80 GPa to 8.54 GPa and a decrease in the indentation hardness from 685.24 MPa to 394.92 MPa. Fig. 6 b) displays the failure envelope at level I for different values of the microporosity for unreinforced geopolymer. The failure domain is bounded by a hyperbola for all values of the microporosity. However, the short and long axes of the hyperbola decrease as the microporosity increases. Similarly, a decrease in the effective friction coefficient is observed as the microporosity increases. Thus, the domain of statically admissible stress states shrinks as the microporosity increases pointing towards a weakening of the material.

3.2. Validation on fiber-reinforced geopolymer composites

We further validate our model using three studies on fiber-reinforced sodium-based and potassium-based geopolymer composites as shown in Fig. 7. In the first two studies, high-tensile modulus basalt fibers are utilized as fillers for potassium-based geopolymer (K-GP). The initial study by Rill et al. [47] considered a single length of fibers, 1/4 inch. In contrast, the later study by Musil and kriven [48] considered two fiber lengths: 1/4 inch and 1/2 inch. The third study utilizes polypropylene (PP) fibers as reinforcement for sodium-based geopolymer (Na-GP) [50].

Fig. 7 compares experimental measurements to our theoretical model, shown using solid curves. The elasto-plastic characteristics for both basalt and polypropylene fibers were reported in the scientific literature as shown in Table 3. The fibers are modelled as a cohesive frictionless inclusion phase due to the symmetry of behavior in tension and in compression. The fibers elasto-plastic constants are then employed to match the experiments with the theory assuming a linear evolution of the microporosity. The average relative error is of 16% for the initial study by Rill et al. on K-GP/basalt fiber composites, 17% for the later study by Musil and Kriven on K-GP/basalt fiber composites, and 5% for Na-GP/polypropylene fiber composites. The average

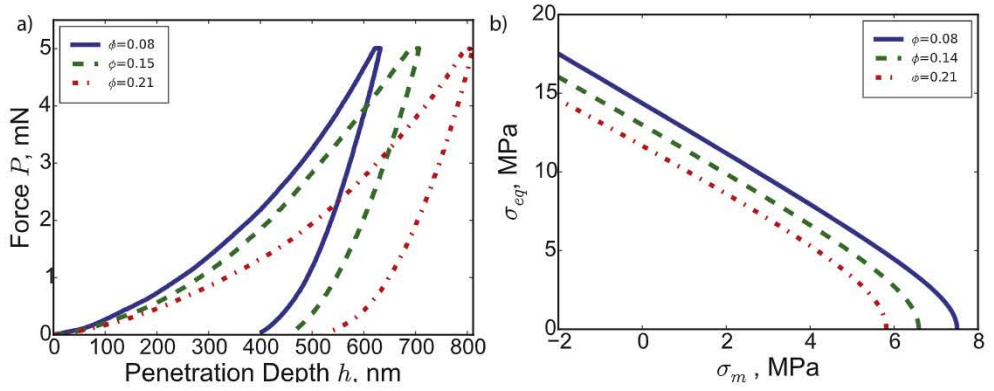

Fig. 6. Influence of microporosity on failure behavior of pure geopolymer. a) Indentation tests b) Failure envelope.

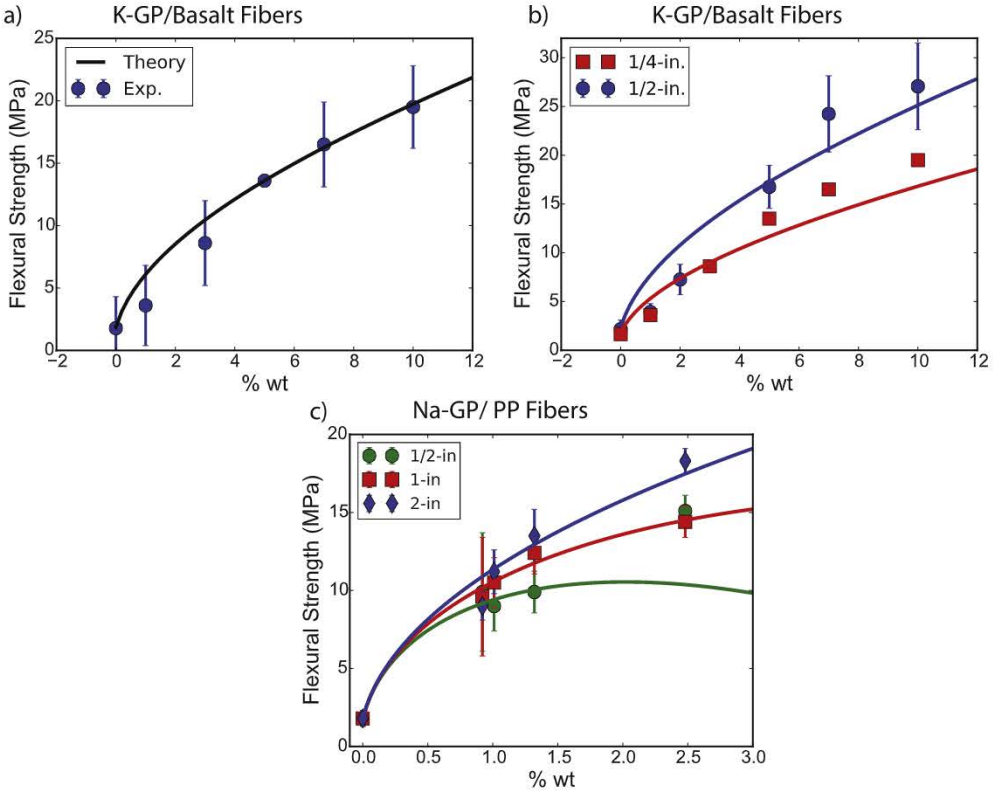

Fig. 7. Model validation for fiber-reinforced geopolymer composites. The data points indicate experimental measurements whereas the solid continuous lines indicate the theoretical predictions. a) Basalt fiber-reinforced potassium-based geopolymer based on the experiments by Rill et al. 2010 [47]. b) Basalt fiber-reinforced potassium geopolymer based on the experiments by Musil and Kriven 2013 [48]. c) Polypropylene (PP)-reinforced sodium-based geopolymer based on the experiments by Lowry and Kriven 2010 [50].

Table 3
Material parameters used for basalt fibers, polypropylene (PP) fibers, and granite particles. ρ is the density in g/cc whereas E is the Young's modulus in GPa. A Von Mises criterion is considered for basalt and polypropylene (PP) fibers. A Drucker-Prager criterion is considered for granite particles. Finally, a hyperbolic criterion is considered for chamotte particles.

Filler	ρ	*E*	Plastic constants	Ref.
Basalt	2.67	84.0	c = 1058.0 MPa	[48]
PP	0.91	1.4	c = 45.0 MPa	[51]
Granite	2.75	85.7	(c = 30.9 MPa, α = 0.75)	[52], This Work
Chamotte	2.0	25	(A = 87.4 MPa, S = 89.1 MPa, B/A = 0.83)	[53]

relative error is comparable to the relative uncertainty of the measurements which is equal to 22% for K-GP/basalt fiber composites and 18% for Na-GP/polypropylene fiber composites. Thus, a good agreement is observed between theory and experiments.

The presence of basalt and polypropylene fiber reinforcement yields a continuous and monotonic evolution of the flexural strength. The continuity is due to the cohesive frictionless behavior of the filler phase. The presence of a cohesive frictionless inclusion phase affects only the size of the failure envelope of the effective material and not the shape or the location of the failure envelope. The monotonic evolution is due to the cohesion of the reinforcement, which is much higher than that of the geopolymer solid skeleton. Nevertheless, in the case of 1/2-inch PP fiber-reinforced Na-GP composites, our model predicts an initial increase of the effective strength followed by a decrease due to the large values of the porosity after a saturating weight fraction of 1.8%.

A strong size effect is observed as the effective strength of the fiber-reinforced geopolymer composites depends on the fiber length. In general, the longer the fiber, the stronger the effective composite. 1/2-inch fiber-reinforced basalt/K-GP composites exhibit a higher strength than 1/4-inch fiber-reinforced basalt-K-GP composites. Similarly, 2-inch fiber-reinforced polypropylene Na-GP composites are stronger than 1-inch fiber-reinforced polypropylene Na-GP composites and 1/2-inch fiber-reinforced polypropylene/Na-GP composites.

The observed size-dependence of the effective strength behavior can be explained by the microporosity φ. In our model, we adopt a linear evolution for the microporosity with respect to the weight fraction of filler: $\varphi = \lambda_1(\%wt) + \lambda_2$. The linear evolution captures the air voids due to potential debonding around the fibers. In the extreme case of a constant microporosity, $\lambda_1 = 0$, perfect bonding exists between the fibers and the geopolymer matrix and the constant microporosity results from the mixing procedure. For instance, in the case of basalt fibers, a silane coating agent was employed to maximize bonding at the interface between the fibers and the amorphous nanoporous geopolymer matrix [47,48].

Our model predicts a less porous microstructure for larger fiber length values. Table 4 displays the computed values of the linear coefficient λ_1 and the offset λ_2. The computed linear coefficient λ_1 is

Table 4
Microporosity parameters computed for basalt fibers, polypropylene (PP) fibers, and granite particles. %wt represent the mass fraction of fillers. For both granite and chamotte fillers, the function shown is valid for strictly positive values of the filler weight fraction, (%wt) > 0.

Filler type	Filler size	Microporosity φ
Rill et al., 2010		
Basalt	1/4-inch	$\varphi = 1.00\ 10^{-5}$ (%wt) + 0.4876
Musil and Kriven 2013		
Basalt	1/4-inch	$\varphi = 1.00\ 10^{-5}$ (%wt) + 0.4881
Basalt	1/2-inch	$\varphi = 1.00\ 10^{-5}$ (%wt) + 0.4781
Lowry et al., 2010		
PP	1/2-inch	φ = 10.17 (%wt) + 0.3383
PP	1-inch	φ = 4.03 (%wt) + 0.3383
PP	2-inch	φ = 0.00 (%wt) + 0.3383
Roper and Kriven 2016		
Raw granite	2-inch	$\varphi = 1.93\ 10^{-1}$ (%wt) + 0.3096
Fine granite	2-inch	$\varphi = 1.96\ 10^{-1}$ (%wt) + 0.2346
Musil and kriven 2014		
Chamotte	N. A.	$\varphi = 8.73\ 10^{-2}$ (%wt) + 0.4262

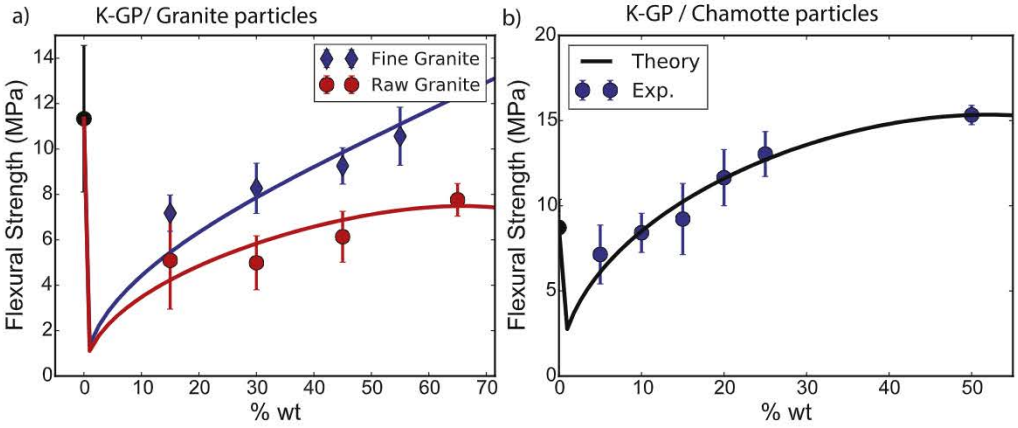

Fig. 8. Model validation for particle-reinforced geopolymer composites. The data points indicate experimental measurements whereas the solid continuous lines indicate the theoretical predictions. a) Granite particle-reinforced potassium-based geopolymer based on the experiments by Roper and Kriven 2016 [49]. b) Chamotte particle-reinforced potassium geopolymer based on the experiments by Musil and Kriven 2014 [44].

positive, ranging from 0.00 to 10.17. Thus, the presence of fiber reinforcement contributes to an increase in microporosity. λ_1 tends to decrease as the fiber length is increased. Thus, larger microporosity values are computed for smaller fiber length values. Small fibers offer a smaller continuous contact area compared to long fibers and consequently result in diminished bonding with the surrounding geopolymer matrix. Moreover, the computed constant offset, λ_2, ranges from 34% to 49% pointing to a very porous microstructure. For basalt fiber, the high value of the computed porosity reflects the mixing process: the fibers were incorporated manually in the initial study by Rill et al. [47] and with a low-speed shear mixing in the later study by Musil and Kriven [48]. Both mixing methods, manual mixing and low-speed shear mixing, resulted in a large amount of entrapped air bubbles. Thus, our model suggests that in order to achieve large gain in the effective strength, it is important to devise a means to maintain low values of the microporosity during the mixing procedure.

3.3. Model validation on particulate geopolymer composites

Next, we validate our model on granite particle-reinforced and chamotte particle-reinforced potassium-based geopolymer composites as displayed in Fig. 8. In the first study, both fine and raw granite particle are used as reinforcement whereas the second study utilizes as a filler phase chamotte particles with a high concentration of SiO_2 and Al_2O_3. We carried out nanoindentation tests on granite particles embedded in a K-GP amorphous geopolymer matrix. A 10×10 series of depth-controlled indentation tests was carried out on granite with a maximum depth of 400 nm, a loading/unloading phase of 30 s and a holding phase of 10 s. The measured indentation modulus was equal to 91.47 MPa and the measured indentation hardness was equal to 5.38 GPa. Using hardness-cohesion relationships for Drucker-Prager materials developed by Ganneau et al. [54],[3] we can then derive the plastic parameters for the granite phase. As for the chamotte phase, a hyperbolic strength criterion was selected so as to yield the tabulated values of the tensile and compressive strength [53]. Fig. 8 compares the predictions of our theoretical model with experimental values. The relative error is 5% for K-GP/chamotte particulate composites and 8% for K-GP/granite particulate composites. Thus, a good agreement is observed between theory and experiments.

For both chamotte and granite, there is a discontinuity in behavior between unreinforced geopolymer with a zero weight fraction of particles and particulate geopolymer composites with a positive weight fraction of particles. The discontinuity results in an initial strength loss for low values of the particle weight fraction. The discontinuity is due to the difference in stress states between pure geopolymer and particulate geopolymer composites. In pure geopolymer, there is a single eigenstress τ_I due to thermal strains within the nanoporous and amorphous geopolymer matrix. In contrast, in particulate geopolymer, there is an additional eigenstress τ_2 due to thermal strains within the inclusion phase. For low values of the particle weight fraction, the two prestresses can have a mutual negative effect, resulting in low values of the effective strength.

Moreover, the processing bears an influence on the effective strength. In the case of granite particle-reinforced geopolymer, two types of fillers were considered: raw and unprocessed granite particles and fine granite particles. The fine granite particles were wetted with water, sieved to a maximum particle size of 90 μm, dried and then crushed. Therefore, due to the processing, the fine granite particles exhibited a smaller diameter and a lower value of the inter-granular porosity compared to raw granite particles. As shown in Table 4, this additional processing step results in lower values of the overall microporosity and higher values of the effective strength for the particulate geopolymer composites.

4. Discussion

4.1. Model predictions for geopolymer foams

Our model enables us to predict the behavior of porous monolithic geopolymer matrices. A key element of our approach is dividing the overall porosity into nanopores and micropores. Let's consider a matrix-pore morphology with low values of the nanoporosity and let's assume a negligible level of interaction between air voids: $\xi = 0$ and $\gamma^{(I)} = 0$. In that case, the effective yield criterion at level I is a Drucker-Prager criterion with an effective friction coefficient $\alpha^{(I)}$ and an effective cohesion $c^{(I)}$. Fig. 9 a) illustrates the evolution of the failure domain as a function of the nanoporosity ϕ in the case ($\nu_s = 0.22$, $\alpha_s = 0.7$) and for a metakaolin potassium-based phase. The effective cohesion $c^{(I)}$ decreases as the nanoporosity ϕ increases. As a result, the domain of statically admissible stress states shrinks as the nanoporosity increases.

We can extend this approach to predict the behavior of geopolymer foams, characterized by both a value of the nanoporosity ϕ and a value of the microporosity φ. Fig. 9b) and c) display the evolution of the Young's modulus and of the uniaxial compressive strength as a function of both the nanoporosity $\phi = 0.36 - 0.41$ and the microporosity $\varphi = 0 - 0.5$ for metakaolin potassium-based geopolymer. For a given value of the nanoporosity, the effective modulus of elasticity and the effective uniaxial compressive strength decrease as the microporosity increases. For a given value of the microporosity, the modulus of elasticity decrease as the nanoporosity increases. The trend is reversed

[3] For tests with a Berkovich probe, given a Drucker-Prager material of cohesion c and friction coefficient α, Ganneau emph et al. solution connects the indentation hardness H to the plastic parameters via.

$$\frac{H}{c} = 4.76(1 + 2.59\alpha + (2.19\alpha)^3 + (1.68\alpha)^{10})$$

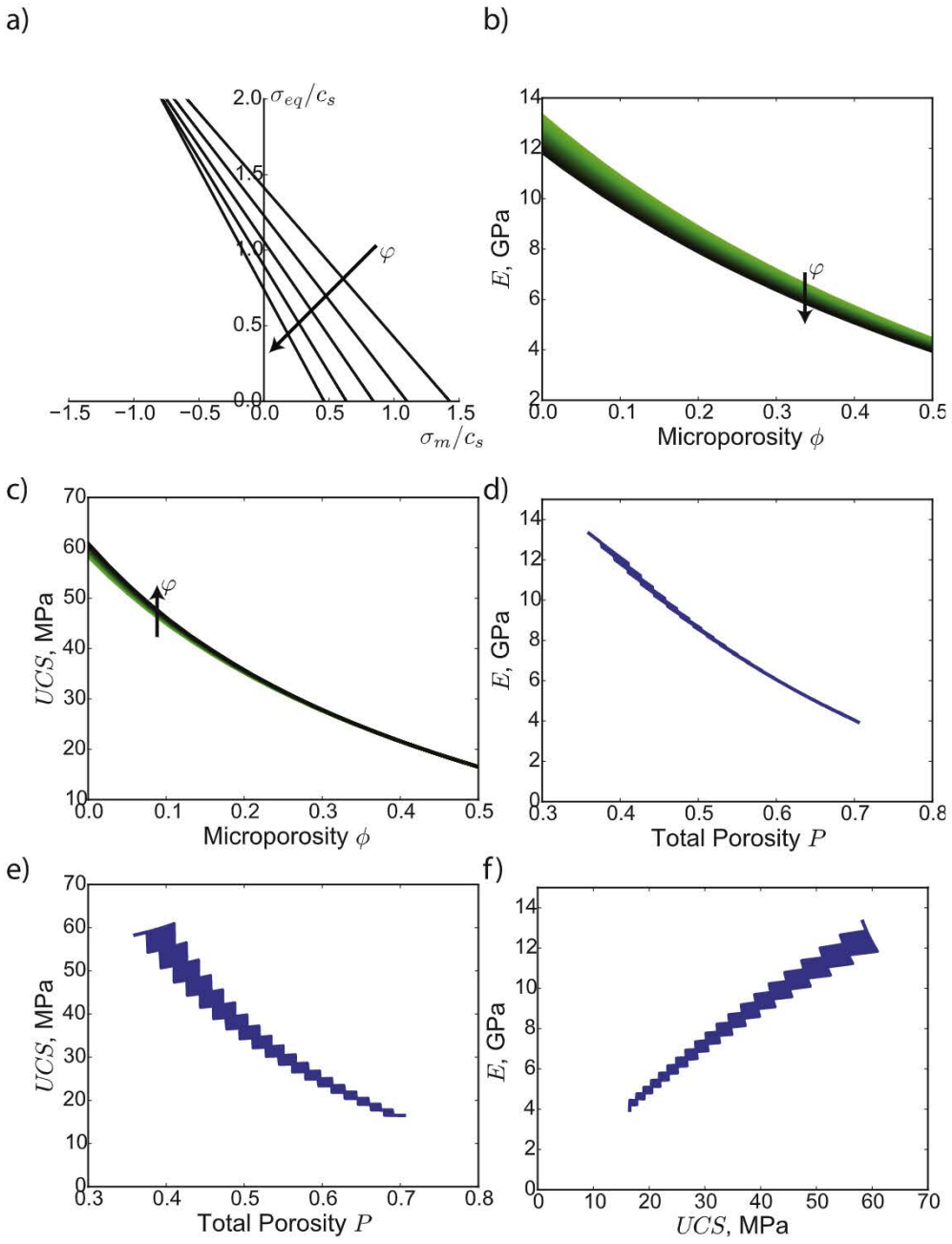

Fig. 9. Influence of nanoporosity and microporosity on strength response of unreinforced metakaolin potassium geopolymer. a) Failure envelope for the amorphous and nanoporous geopolymer matrix for low values of the nanoporosity. b) Evolution of the effective modulus of elasticity E as a function of the nanoporosity ϕ and of the microporosity φ. c) Influence of the nanoporosity ϕ and of the microporosity φ on the effective uniaxial compressive strength UCS. d) Influence of total porosity $P = \varphi + (1 - \varphi)\phi$ on the elastic modulus E. e) Influence of total porosity $P = \varphi + (1 - \varphi)\phi$ on the uniaxial compressive strength. f) Effective modulus of elasticity E as a function of the effective uniaxial compressive strength UCS.

for the uniaxial compressive strength, which increases as the nanoporosity increases, under fixed microporosity. These trends highlight the sources of energy dissipation in porous unreinforced geopolymers. Nanopores provide actives means of energy dissipation through free volume changes, contributing to an improvement in the overall strength. Meanwhile, micropores act as stress concentrators, resulting in a detrimental effect on the effective strength. Both nanopores and micropores inhibit the material's ability to store mechanical strain energy through reversible deformations such as volume changes and rotations, leading to a decrease in the macroscopic elastic modulus.

An important question is to explore the applicability to porous unreinforced geopolymers of classic strength-porosity empirical models developed for porous glass [55], powder metals [56], porous ceramics [57], and for porous materials [58] as displayed in Table 5. Hasselman's model predicts a linear evolution whereas Balshin's model predicts a power-law evolution, Ryshkewith ‘s model predicts an exponential law, and Schiller's model predicts a logarithmic decrease of the strength with respect to the porosity. These four models exhibit three common features: (i) the main variable is the porosity p irrespective of the pore size, (ii) a one-to-one matching is expected between the strength and the porosity, and (iii) the porosity is expected to exert a negative influence on the effective strength. In contrast, geopolymers exhibit a dual porosity with a nanoporosity and a microporosity. As shown in Fig. 9 e) there is not a unique correspondence between the effective strength and the total porosity P. Given a value of the total porosity P, there is a spectrum of plausible values of the effective

Table 5
Classic mechanical performance-porosity models proposed for porous materials. p is the porosity. UCS is the uniaxial compressive strength in MPa. E is the macroscopic Young's modulus in GPa. φ is the microporosity, ϕ is the nanoporosity and $P = \varphi + (1-\varphi)\phi$ is the total porosity. K-GP = metakaolin potassium geopolymer.

Author	Equation	Model constants
Strength-Porosity		
Hasselman [55]	$UCS = UCS_0(1 - bp)$	UCS_0, b
Balshin [56]	$UCS = UCS_0(1-p)^n$	UCS_0, n
Ryshkewith [57]	$UCS = UCS_0 \exp(-np)$	UCS_0, n
Schiller [58]	$UCS = k \log(p_0/p)$	k, p_0
This work	$UCS \approx 58.99 \exp(-2.53\varphi)$	valid for K-GP foams.
Stiffness-Porosity		
Rice [59]	$E = E_0 \exp(-tp)$	E_0, t
Kendall [60]	$E = E_0(1-p)^3$	E_0
This work	$E \approx 47.57 \exp(-3.41P)$	valid for K-GP foams.

strength depending on the decomposition of the total porosity P into nanoporosity ϕ and microporosity φ. Moreover, the nanoporosity actually contributes to an improvement in strength properties. Thus, classic models that do not account for the pore size are not directly applicable to geopolymer matrices. Nevertheless, an approximate one-to-one matching can be established when the total porosity is replaced by the microporosity φ, as shown in Fig. 9 c). In this case, the Ryshkewith's model provides the best approximation with: $UCS \approx 58.99 \exp(-2.53\varphi)$ and with a coefficient of determination $R^2 = 0.9992$.

Similarly, we compared the predictions of our model to classic stiffness-porosity relationships developed for porous ceramics and cementitious materials. For instance, Rice's equation [59] predicts an exponential decline of the effective modulus with the porosity whereas Kendall's model [60] predicts a power-law evolution. As shown in Fig. 9 b) and d), although the effective Young's modulus E varies as a function of both the nanoporosity ϕ and the microporosity φ, there is an approximate one-to-one correspondence between the macroscopic Young's modulus and the total porosity. In the case of metakaolin-based potassium geopolymer with Si/Al = 2, Rice's model yields the optimal parameters: $E \approx 47.57\exp(-3.41P)$ with a coefficient of determination $R^2 = 0.9977$.

4.2. Influence of processing on microporosity

There is a strong influence of the processing on the strength behavior of pure geopolymer. Three types of processing, corresponding to three studies, are considered as shown in Table 6. In the first study by Rill et al. [47], a shear mixer was used to mix the alkaline solution and the aluminosilicate source. In the second study by Musil and Kriven [48], the shear mixing step was followed by vibration using an orbital shaker table. In the third study by Roper and Kriven [49], a final step was added after shear mixing and vibrating: mixing and degassing in a centrifugal mixer. Shear mixing resulted in a flexural strength of 1.7 MPa, whereas shear mixing and vibrating yielded a material with a higher flexural strength of 2.2 MPa. Finally, combining shear mixing and vibrating with centrifugal mixing and degassing yielded the highest flexural strength value, 11.33 MPa. Thus, the vibrating and degassing steps represent effective means to improve the mechanical performance of geopolymer.

Table 6
Influence of processing on strength characteristics of pure potassium geopolymer (K-GP). σ_0 is the measured flexural strength whereas φ is the computed microporosity.

Mixing Procedure	σ_0 (GPa)	φ (%)	Ref.
Shear mixer	1.7	82	[47]
Shear mixer and vibration table	2.2	78	[48]
Shear mixer, vibration table, and centrifugal mixing and degassing	11.33	4	[49]

The observed improvement in mechanical performance is linked with a decrease of the microporosity with processing. As shown in Table 6, the shear mixing specimen exhibits a high value of the computed microporosity, 82%, pointing to entrapped macroscopic voids. In contrast, vibrating contributes to the removal of macroscopic air voids. As a result, the computed microporosity value for specimen 2 (vibrating table) is significantly lower: 78%. The lowest microporosity value, 4%, is observed for specimen 3, after centrifugal mixing and degassing. This very small value idicates that centrifugal degassing is a powerful means to eliminate both macroscopic and microscopic air voids.

Our physics-based mechanistic model enables us to quantify the potential gains for improved processing procedure. Fig. 10 displays the actual and the potential evolution of the uniaxial compressive strengths for metakaolin potassium geopolymer reinforced with granite particles, chamotte particles and basalt fibers. For both granite and chamotte particle, we investigate the potential strength enhancement following a 10%, 20%, and 30% reduction in microporosity. For basalt fiber-reinforced composites, we investigate the potential strength enhancement following a 2%, 5%, and 10% reduction in microporosity. The microporosity is controlled by the processing method: in this case, one route to meet these targets would be to increase the magnitude and duration of the vibrations after mixing in the reinforcement using a shear mixer.

For all composites, a simple reduction in microporosity is linked in tremendous gain in uniaxial compressive strength. For instance, in Granite/K-GP a 10% reduction in mciroporosity results in a 7%-18% gain in strength, a 20% reduction in microporosity results in a 14%-36% gain in strength, and a 30% reduction in microporosity leads to a 22%-53% gain in strength. The gains in strength are even higher for chamotte/K-GP and basalt fiber/K-GP composites. For chamotte/K-GP composites, a 10% reduction in microporosity leads to a 36%-119% gain in strength, a 20% reduction in microporosity leads to a 66%-203% gain in strength, and a 30% reduction in microporosity leads to a 94%-275% gain in strength. For basalt fiber/K-GP composites, a 2% improvement in microporosity leads to a 22%-26% increase in strength, a 5% improvement in microporosity leads to a 53%-62% gain in strength, and a 10% reduction in microporosity leads to a 100%-125% increase in strength. These figures highlight the role of micropores as stress concentrators. These figures also underline the fact that geopolymer composites are both ceramics and granular materials.

4.3. Influence of alkali concentration on behavior of geopolymer skeleton

Next we investigate the effect of the alkali concentration on the strength domain of pure geopolymer. The chemical composition of the potassium geopolymer (K-GP) is $K_2O\ Al_2O_3 4SiO_2 11H_2O$ and the chemical composition of the sodium geopolymer is $Na_2O\ Al_2O_3 4SiO_2 11H_2O$. Table 7 lists the computed elasto-plastic characteristics of the geopolymer skeleton at the molecular lengthscale for both type of alkali cations, K^+ or Na^+. The nanoporosity is drawn from mercury intrusion porosimetry tests [24] and gas physical adsorption tests [25] carried out by Kriven et al.. We further assume that both pure potassium geopolymer and pure sodium geopolymer exhibit similar values of the internal friction coefficient α_s and of the Poison's ratio ν_s. Thus, we calculated the remaining elasto-plastic constants using the vast database of experimental tests.

The computed elasto-plastic characteristics, $(m_s, \nu_s, c_s, \alpha_s)$ represent optimized parameters that enabled us to reproduce the observed experimental data in our nanoindentation experiments, see Fig. 5, and in the macroscopic characterization tests conducted by Kriven and coworkers on both fiber-reinforced [44,47,48,50] and particle-reinforced geopolymer composites [44,49]. Thus, the mechanical characteristics of the geopolymer skeletons were computed using a set of $N_1 = 36$

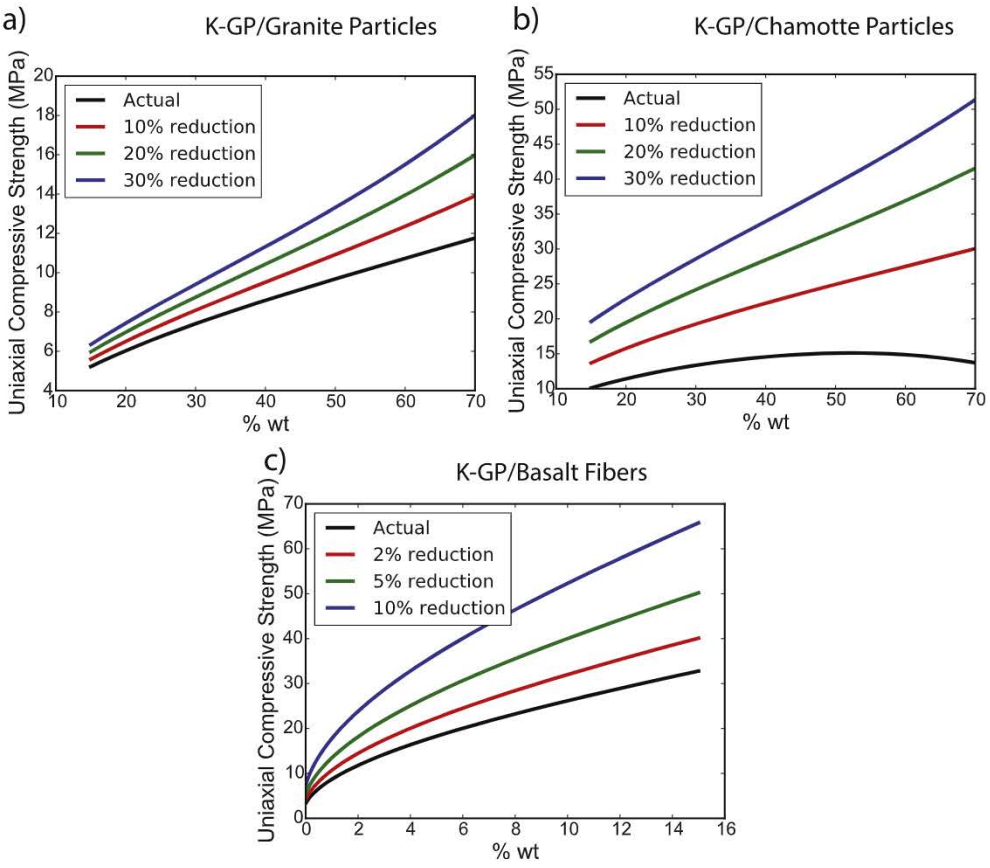

Fig. 10. Predicted uniaxial compressive strength using the actual processing procedure and for improved method resulting in a reduction in microporosity. a) K-GP/granite composites for the actual microporosity and in case of a 10%, 20%, and 30% reduction in microporosity. b) K-GP/chamotte composites for the actual microporosity and in case of a 10%, 20%, and 30% reduction in microporosity. c) K-GP/basalt composites for the actual microporosity and in case of a 2%, 5%, and 10% reduction in microporosity.

Table 7
Skeleton characteristics of potassium-based geopolymer (K-GP) and sodium-based geopolmyer (Na-GP).

Geopolymer	m_s (GPa)	ν_s	c_s (MPa)	α_s	ϕ
K-GP	28.00	0.22	17.50	0.76	40
Na-GP	16.30	0.22	4.22	0.76	40

potassium-based geopolymer composites and $N_2 = 12$ sodium-based geopolymer composites and relying on >544 experimental tests at both the nanometer and the macroscopic lengthscales.

Overall, our computations suggest that pure potassium-based geopolymer is stiffer and stronger than pure sodium-based geopolymer. The computed plane strain modulus of the potassium geopolymer skeleton is higher than that of the sodium geopolymer skeleton. The computed cohesion of the potassium geopolymer skeleton is more than two times higher than that of the sodium geopolymer skeleton. Our findings are in agreement with the experiments of Duxson [9] who found a strong influence of the chemistry on the mechanical behavior. More generally for varying Si/Al ratios and in the absence of unreacted phases, the Si/Al ratio and the alkaline concentration will affect the nanostructure and elastoplastic characteristics of the skeleton at the molecular level. The case of unreacted phases is treated separately.

Thus, our model supports the notion of an intrinsic skeleton at the molecular level whose nanostructure and mechanical properties depend solely on the chemical composition—Si/Al ratio, alkaline concentration, and aluminosilicate source—irrespective of the curing temperature or mixing conditions, as suggested by Smilauer and coworkers [14]. Our initial calculations confirm the strong influence of the chemistry on the mechanical behavior even at the molecular level. Moreover, our approach provides a means to predictively correlate the pore structure to the effective behavior for geopolymer composites.

4.4. Unreacted phases

One of the advantages of geopolymers is the option to use natural sources of aluminosilicates such as fly ash or slag. However, due to the presence of impurities, fly ash and slag usually result in the presence of unreacted phases. An important question is to understand the contribution of those unreacted phases to mechanical energy storage and dissipation mechanisms. Three cases need to be considered as discussed below.

Case 1: the unreacted phases remain in powder form without any significant bonding to the solid material. This would mean that the unreacted phases can be flushed out of the material by mere washing. In that case, these unreacted phases will occupy micropores and will behave essentially as air voids. Thus, the current model can be applied where this time the micropore phase includes both empty pores and pores filled with unreacted material.

Case 2: the unreacted phases have bonded to the solid material. This can happen if gel nucleation occurs at the grain boundaries of unreacted material. As illustrated in Fig. 11a), the unreacted material constitutes a phase in the conceptual model at level II. If the unreacted material exhibits a cohesive frictionless behavior, then Eqs. (36) and (37) can be modified so as to include the unreacted material phase. If the unreacted material exhibits a cohesive frictional behavior, there is an additional prestress term due to thermal strains within the unreacted material phase and new theoretical solutions must be derived.

Case 3: there is more than one major reaction product. If the geopolymerization reaction leads to two reaction products that are different in terms of chemical composition or in terms of microstructure—for instance low-density versus high-density—, then the conceptual model needs to be altered. Fig. 11 b) illustrates the altered conceptual model to consider the case of two geopolymer reaction phases, GP1 and GP2, that are themselves nanoporous. In that case, the upscaling process is more involved as the behavior of each reaction

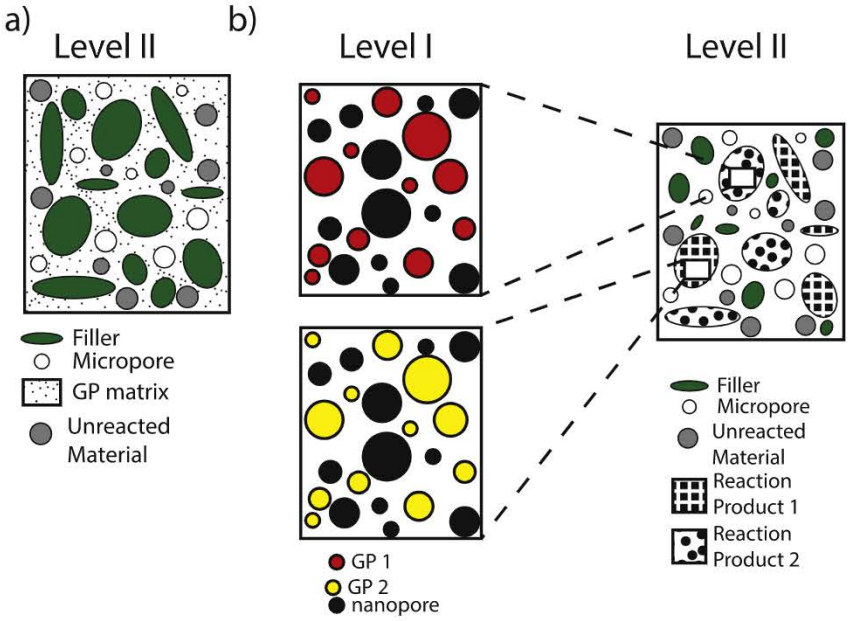

Fig. 11. Influence of unreacted phases on energy storage and energy dissipation mechanisms of geopolymer composites.

phase must be resolved at level I and the output needs to be integrated at level II to predict the constitutive response of the resulting composite. Such a multiscale upscaling approach can be carried out using analytical methods or using computational methods. Nevertheless, the physics-based conceptual framework that we have introduced can be extended to include a broad class of geopolymer composites–such as fly ash-based geopolymer composites— and connect the effective constitutive response at large scale to the physics of the materials at lower lengthscales.

5. Conclusions

- We introduce a novel physics-based mechanistic framework to understand the influence of heterogeneity and porosity on the mechanical behavior of geopolymer composites. A four-level multiscale conceptual model is formulated for geopolymer composites that makes it possible to pinpoint the contribution of different phases to the effective mechanical response. Due to the nanogranular microstructure of the geopolymer gel at the molecular level, geopolymer composites exhibit a distinctly granular mechanical response.
- We introduce a distinction between nanoporosity and microporosity. The idea is that air voids, depending on their size, affect the mechanical response differently. Micropores act as stress concentrators and are detrimental to strength development. Meanwhile, nanopores provide additional energy dissipation mechanisms via free volume changes and provide a slight enhancement in strength. There is an approximate one-to-one matching between the effective strength and the microporosity whereas there is an approximate matching between the effective stiffness and the total porosity.
- Both the microporosity and the nanoporosity are controlled by different parameters. For instance, the nanoporosity in controlled by the chemistry of the geopolymer binder and in turn the nanoporosity affects the response at the microscopic level of level I. The nanoporosity is not influenced by the processing method or by the presence of fillers. Meanwhile, the microporosity is controlled by the mixing procedure, the filler shape and type, and the microporosity in turn control the behavior at the mesoscale and the macroscopic level. Our theoretical approach enables us to rank processing methods according to their effectiveness. Moreover, our theoretical approach is able to quantitatively predict the strength improvement following a reduction in microporosity.
- In the case of metakaolin-based polysialate siloxo geopolymers with a ratio Si/Al = 2, analytical solutions are formulated to describe the elastic and strength response of geopolymer composites. The theoretical solutions predict the behavior as a function of the effect of mix design, processing method, and alkali activator for both particle- and fiber-reinforced geopolymer composites. Our analytical solutions are validated using an ample dataset of >544 experiments

Overall, our investigation is an important step in the mechanistic modeling of the behavior of geopolymer composites so as to advance the science and technology of geopolymer composites.

Acknowledgments

This material is based upon work supported by the National Science Foundation under Grant No. CMMI 1727922. This research is part of the Blue Waters sustained-petascale computing project, which is supported by the National Science Foundation (awards OCI-0725070 and ACI-1238993) and the state of Illinois. Blue Waters is a joint effort of the University of Illinois at Urbana-Champaign and its National Center for Supercomputing Applications. This research was supported in part through the computational resources and staff contributions provided for the Quest high performance computing facility at Northwestern University which is jointly supported by the Office of the Provost, the Office for Research, and Northwestern University Information Technology.

References

[1] J. Davidovits, Recent progresses in concretes for nuclear waste and uranium waste containment, Concr. Int. 16 (1994) 53–58.
[2] J. Davidovits, Environmentally driven geopolymer cement applications, Proceedings of 2002 Geopolymer Conference. Melbourne. Australia, 2002.
[3] P. Duxson, A. Fernndez-Jimnez, J.L. Provis, G.C. Lukey, A. Palomo, J.S.J. Van Deventer, Geopolymer technology: the current state of the art, J. Mater. Sci. 42 (2007) 2917–2933.
[4] P. Suraneni, S. Puligilla, E.H. Kim, X. Chen, L.J. Struble, P. Mondal, Monitoring setting of geopolymers, Adv. Civ. Eng. Mater. 3 (2014) 177–192.
[5] D.C. Comrie, J.H. Paterson, D.J. Ritchey, Geopolymer technologies in toxic waste management, Proceedings of the 1st European Conference on Soft Mineralogy (Geopolymer 1988), Compiegne, France, 1988.
[6] D.P. Dias, C. Thaumaturgo, Fracture toughness of geopolymeric concretes reinforced with basalt fibers, Cement Concr. Compos. 27 (2005) 49–54.
[7] A. Natali, S. Manzi, M.C. Bignozzi, Novel fiber-reinforced composite materials based

on sustainable geopolymer matrix, Procedia Eng 21 (2011) 1124–1131.
[8] P. Duxson, J.L. Provis, G.C. Lukey, S.W. Mallicoat, W.M. Kriven, J.S. Van Deventer, Understanding the relationship between geopolymer composition, microstructure and mechanical properties, Colloids Surf. A Physicochem. Eng. 269 (2005) 47–58.
[9] P. Duxson, S.W. Mallicoat, G.C. Lukey, W.M. Kriven, J.S. van Deventer, J.S, The effect of alkali and Si/Al ratio on the development of mechanical properties of metakaolin-based geopolymers, Colloids Surf. A Physicochem. Eng. 292 (2007) 8–20.
[10] B.A. Fillenwarth, S.M. Sastry, Development of a predictive optimization model for the compressive strength of sodium activated fly ash based geopolymer pastes, Fuel 147 (2015) 141–146.
[11] M. Ghanbari, A.M. Hadian, A.A. Nourbakhsh, K.J.D. MacKenzie, K.J.D, Modeling and optimization of compressive strength and bulk density of metakaolin-based geopolymer using central composite design: a numerical and experimental study, Ceram. Int. 43 (2017) 324–335.
[12] A. Nazari, F.P. Torgal, Predicting compressive strength of different geopolymers by artificial neural networks, Ceram. Int. 39 (2013) 2247–2257.
[13] M.M. Yadollahi, A. Benli, R. Demirboga, Application of adaptive neuro-fuzzy technique and regression models to predict the compressive strength of geopolymer composites, Neural Comput. Appl. 28 (2017) (2017) 1453–1461.
[14] V. Šmilauer, P. Hlaváček, F. Škvára, R. Šulc, L. Kopecký, J. Němeček, Micromechanical multiscale model for alkali activation of fly ash and metakaolin, J. Math. Sci. 46 (2011) 6545–6555.
[15] H. Lee, V. Vimonsatit, P. Chindaprasirt, Mechanical and micromechanical properties of alkali activated fly-ash cement based on nano-indentation, Constr. Build. Mater. 107 (2016) 95–102.
[16] K.T. Nguyen, N. Ahn, T.A. Le, K. Lee, Theoretical and experimental study on mechanical properties and flexural strength of fly ash-geopolymer concrete, Constr. Build. Mater. 106 (2016) 65–77.
[17] M.E. Gurtin, E. Fried, L. Anand, The Mechanics and Thermodynamics of Continua, Cambridge University Press, Cambridge, 2010.
[18] S. Timoshenko, J.N. Goodier, Theory of Elasticity, McGraw-Hill Book Company, Inc, London, 1951.
[19] J. Salencon, Applications of the Theory of Plasticity in Soil Mechanics, Wiley, 1977.
[20] F.-J. Ulm, O. Coussy, Mechanics and durability of solids, Mech. Solids I (2002) Prentice-Hall.
[21] J. Davidovits, Geopolymers and geopolymeric materials, J. Therm. Anal. 35 (1989) 429–441.
[22] J. Davidovits, Geopolymers, J. Therm. Anal. 37 (1991) 1633–1656.
[23] D.C, W. Drucker, W. Prager, Soil mechanics and plastic analysis or limit design, Q. Appl. Math. 10 (1952) 157–165.
[24] W.M. Kriven, J.L. Bell, M. Gordon, Microstructure and microchemistry of fully-reacted geopolymers and geopolymer matrix composites, Ceram. Trans. 153 (2003) 227–250.
[25] W.M. Kriven, J.L. Bell, M. Gordon, Microstructure and nanoporosity of asSet geopolymers. Mechanical properties and performance of engineering ceramics II, Ceram. Eng. Sci. Proc. 27 (2005) 491–503.
[26] D.L.Y. Kong, J.G. Sanjayan, K. Sagoe-Crentsil, Comparative performance of geopolymers made with metakaolin and fly ash after exposure to elevated temperatures, Cem. Conc. Res. 37 (2007) 1583–1589.
[27] M. Gordon, J.L. Bell, W.M. Kriven, Comparison of naturally and synthetically-derived, potassium-based geopolymers, Advances in Ceramic Matrix Composites X: Proceedings of the 106th Annual Meeting of the American Ceramic Society, Indianapolis, Indiana, USA 2004, Ceramic Transactions, 165 Wiley-American Ceramic Society, 2005, p. 95.
[28] T. Lin, D. Jia, M. Wang, P. He, D. Liang, Effects of fibre content on mechanical properties and fracture behaviour of short carbon fibre reinforced geopolymer matrix composites, Bull. Mater. Sci. 32 (2009) 77–81.
[29] S.A. Bernal, J. Bejarano, C. Garzn, R.M. De Gutierrez, S. Delvasto, E.D. Rodrguez, Performance of refractory aluminosilicate particle/fiber-reinforced geopolymer composites, Compos. B Eng. 43 (2012) 1919–1928.
[30] L. Dormieux, D. Kondo, F.-J. Ulm, Micropromechanics, John Wiley & Sons, 2006.
[31] S. Nemat-Nasser, M. Hori, Micromechanics: Overall Properties of Heterogeneous Materials, North-Holland, 1998.
[32] A. Zaoui, Continuum micromechanics: survey, J. Eng. Mech. 128 (2002) 808–816.
[33] E. Grueschow, J.W. Rudnicki, Elliptic yield cap constitutive modeling for high porosity sandstone, Int. Journ. Sol. Struct. 42 (2005) 4574–4587.
[34] J.C. Jaeger, W.G.W. Cook, Fundamentals of Rock Mechanics, Chapman and Hall, London, 1979.
[35] D.R.S. Talbot, J.R. Willis, Variational principles for inhomogeneous non-linear media, IMA Journ. Appl. Mech. 35 (1985) 39–54.
[36] P.P. Castañeda, J.R. Willis, On the overall properties of nonlinearly viscous composites, Proc. Roy. Soc. Lond. A 416 (1988) 217–244.
[37] P.P. Castañeda, The effective mechanical properties of nonlinear isotropic composites, J. Mech. Phys. Sol. 39 (1991) 45–71.
[38] L. Guoan, P.P. Castaeda, The effect of particle shape and stiffness on the constitutive behavior of metal-matrix composites, Int. Journ. Sol. Struct. 30 (1993) 3189–3209.
[39] O. Lopez-Pamies, P.P. Castaeda, P.P, On the overall behavior, microstructure evolution, and macroscopic stability in reinforced rubbers at large deformations: ITheory, J. Mech. Phys. Sol. 54 (2006) (2006) 807–830.
[40] M.M. Zhou, G. Meschke, Strength homogenization of matrix-inclusion composites using the linear comparison composite approach, Int. Journ. Sol. Struct. 51 (2014) 259–273.
[41] M. Vandamme, F.-J. Ulm, P. Fonollosa, Nanogranular packing of CSH at substochiometric conditions, Cem. Conc. Res. 40 (2010) 14–26.
[42] C.P. Bobko, B. Gathier, J.A. Ortega, F.-J. Ulm, L. Borges, Y.N. Abousleiman, The nanogranular origin of friction and cohesion in shalea strength homogenization approach to interpretation of nanoindentation results, Int. Jour. Numer. Anal. Methods Geomech. 35 (2012) 1854–1876.
[43] J.A. Ortega, B. Gathier, F.J. Ulm, F.J, Homogenization of cohesive-frictional strength properties of porous composites: linear comparison composite approach, J. Nanomech. Micromech. 1 (2011) 11–23.
[44] S.S. Musil, W.M. Kriven, W.M, In situ mechanical properties of chamotte particulate reinforced, potassium geopolymer, J. Am. Ceram. Soc. 97 (2014) 907–915.
[45] W.C. Oliver, G.M. Pharr, An improved technique for determining hardness and elastic modulus using load and displacement sensing indentation experiments, J. Mat. Res. 7 (1992) 1564–1583.
[46] A.-T. Akono, Y. Cui, A. Kataruka, K. Anderson, P. Kabir, Intrinsic mechanical properties of calcium aluminate crystals via the linear comparison composite method coupled with nano-indentation, Mech. Mater. 118 (2018) 74–84.
[47] E. Rill, D.R. Lowry, W.M. Kriven, Properties of basalt fiber reinforced geopolymer composites, Cer. Eng. Sci. Proc. 31 (2010) 57.
[48] S.S. Musil, G.P. Kutyla, W.M. Kriven, The Effect of Basalt Chopped Fiber Reinforcement on the Mechanical Properties of Potassium Based Geopolymer, John Wiley & Sons, Inc, Hoboken, NJ, USA, 2012, pp. 31–42.
[49] D.S. Roper, G.P. Kutyla, W.M. Kriven, December. Properties of granite powder reinforced potassium geopolymer, developments in strategic ceramic materials, A Collection of Papers Presented at the 39th International Conference on Advanced Ceramics and Composites, January 25-30, 2015, Daytona Beach, Florida, 604 John Wiley & Sons, 2015, p. 3.
[50] D.R. Lowry, W.M. Kriven, Effect of high tensile strength polypropylene chopped fiber reinforcements on the mechanical properties of sodium based geopolymer composites, Ceram. Eng. Sci. Proc. 31 (2010) 47.
[51] accesed on February 24th 2019 www.matweb.com.
[52] E.Z. Lajtai, A.M. Gadi, A.M, Friction on a granite to granite interface, Rock Mech. Rock Eng. 22 (1989) 25–49.
[53] accessed February 24th 2019 http://www.rupbox.com/material-properties/information/chamotte.
[54] F.P. Ganneau, G. Constantinides, F.J. Ulm, Dual-indentation technique for the assessment of strength properties of cohesive-frictional materials, Int. Journ. Sol. Struct. 43 (2006) 1727–1745.
[55] D.P.H. Hasselman, R.M. Fulrath, R.M, Effect of small fraction of spherical porosity on elastic moduli of glass, J. Am. Ceram. Soc. 47 (1963) 52–53.
[56] M.Y. Balshin, Relation of mechanical properties of powder metals and their porosity and the ultimate properties of porous metal-ceramic materials, Dokl Akad Nauk SSSR, 67 1949, pp. 831–834.
[57] E. Ryshkewitch, Compression strength of porous sintered alumina and zirconia: 9th communication to ceramography, J. Am. Ceram. Soc. 36 (1953) 65–68.
[58] K.K. Schiller, Strength of porous materials, Cem. Conc. Res. 1 (1971) 419–422.
[59] R.W. Rice, Effects of amount, location, and character of porosity on stiffness and strength of ceramic fiber composites via different processing, J. Mat. Sci. 34 (1999) 2769–2772.
[60] K. Kendall, A.J. Howard, J.D. Birchall, The relation between porosity, microstructure and strength, and the approach to advanced cement-based materials, Philos. Trans. Royal Soc. Series A, Mat. Phy. Sci. 310 (1983) 139–153.